Quarterly Report for
January - March 2000
Stanford Geothermal Program
DE-FG07-99ID13763

Table of Contents

1. MEASUREMENTS OF STEAM-WATER RELATIVE PERMEABILITY

This research project is being conducted by Research Assistant Peter O'Connor and Professor Roland Horne. The aim is to measure relative permeability relations for steam and water flowing simultaneously in rock and to examine the effects of temperature, flow rate, and rock type. In the first stage, the experiments will attempt to reproduce results obtained in a previous experiment (Mahiya, 1999), but holding the experimental pressure as close as possible to a constant value.

1.1 BACKGROUND

An X-ray CT technique has been used in recent years to measure the distribution of steam and water saturation in rocks to obtain steam-water relative permeability curves (Satik and Horne, 1998, Mahiya, 1999). Glenn Mahiya conducted his experiment in 22 steps with imbibition and drainage processes across a range of saturation conditions. The resulting relationship for steam-water relative permeability as a function of saturation resembled a Corey function. Since the mass flow rate was almost constant, and since the process was adiabatic but not isothermal, it was difficult to maintain a constant pressure differential. Variations in pressure cause changes in the temperature as well as in the slip factor, which may have contributed to scatter in the steam relative permeability curve.

The current experiment is attempting to maintain a constant pressure, to avoid this difficulty. As the experiment will be constantly at an inlet gauge pressure of 15 psi, it will necessarily be at a constant 120º C at the inlet in order to have two-phase flow throughout, with the rest of the core being at the saturation temperature for the pressure at that point. Our expectation is an identical pressure profile and temperature profile for every step of the process.

The current experiment was begun in January 2000. We are currently awaiting availability of the CT scanner; in the meantime, progress continues. Necessary flow rates are being determined, the heat guard mechanism has been redesigned and is being refined, and defective instrumentation is being replaced.

1.2 EXPERIMENTAL PROCEDURE

The experiments will use the same apparatus used by Mahiya, as shown in Figure 1.1. A Berea sandstone was drained, flushed with nitrogen, then subjected to a vacuum. A dry X-ray scan was made to obtain CT_{dry}. The next step was to saturate the core with water and scan to obtain CT_{wet}; however, the CT scanner failed at this point and this step will be repeated in May 2000. From these scans, a porosity distribution will be obtained, expected to yield an average value of 24.7%. In the next step, hot liquid water is flowed through to obtain CT_{hw}, which is necessary to calculate experimental saturations. The next steps are the actual flow-through experiments. The core will be under a pressure gradient of approximately 15 psi across the 41-cm length. First, the core will be saturated with steam. Steam flow rate will be lowered gradually in 10% increments, to implement an imbibition process whereby the wetting phase (water) displaces the nonwetting phase

(steam). A flexible heat guard ensures negligible overall heat loss for a near-adiabatic process. The flexible heat guard control mechanism was redesigned this year. At each step, the system will reach a steady state and will then be subject to CT scan to measure saturation. Steam flow rate will be reduced to 0%, then increased. This second sequence will be a drainage process.
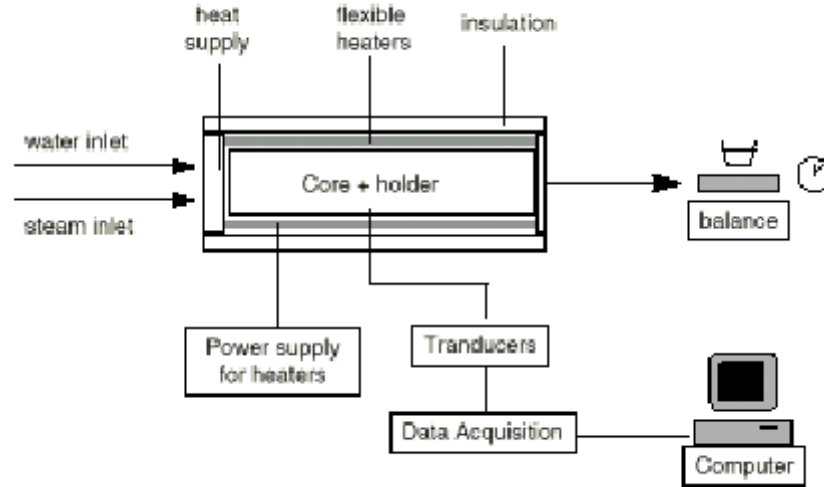
Figure 1.1: Schematic of flow-through relative permeability experiment.

At every stage, pressure, temperature and heat fluxes from the core are to be measured. Calculated relative permeability to steam and water are then plotted against the saturation measurements. The major suggested change from the previous experiment is to perform the imbibition step first. Performing the imbibition step first allows determination of the maximum pressure. This pressure can be maintained by increasing flow rates if necessary.

The current experimental procedure involves finding the correct flow rates and power inputs to ensure a pressure differential of 15 psi and a temperature at the inlet of slightly over 120º C for the steam, and slightly under 120º C for the hot water. As a preliminary step, we have estimated the necessary rates using numerical simulation, as shown in Figure 1.2. In this procedure, we determine pairs of flow rates for water and steam, at different ratios, to result in steady-state flow with a pressure differential of 15 psi. This process also determines the heater settings (voltage and current). All that is unknown is the saturation; once the CT scanner is available, it should be a simple matter to determine the saturation. The base values used are derived from Glenn Mahiya's experiment, considering the existing pressure gradient for a given set of water and steam flow rates and scaling to a 15 psi gradient. Further refinement of the values is determined experimentally.
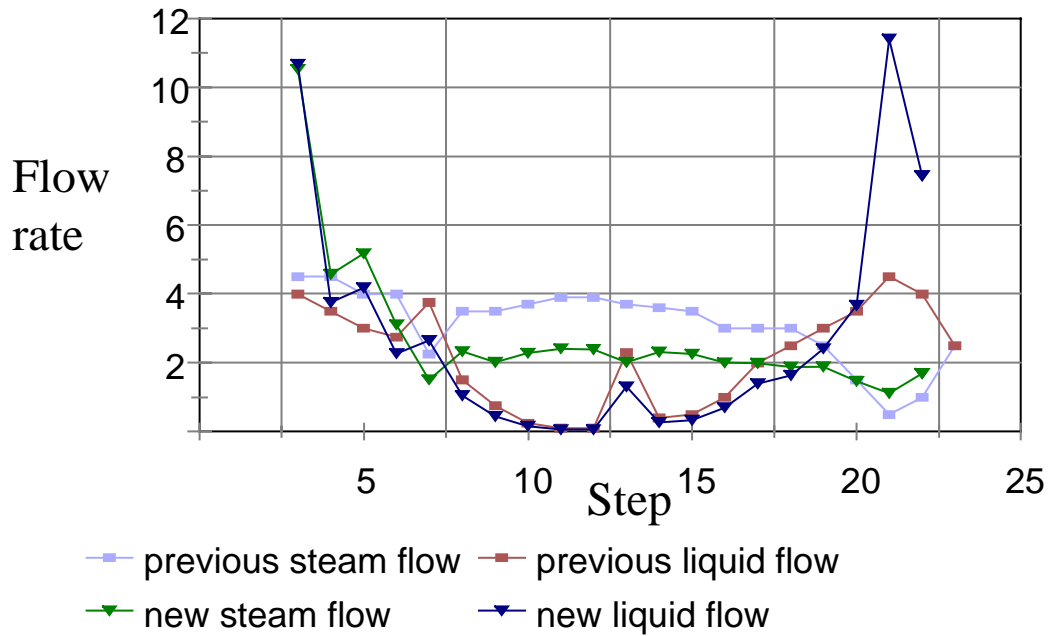
Figure 1.2: Simulated flow rates required to maintain constant pressure drop, compared to the flow rates used in Mahiya's experiments.
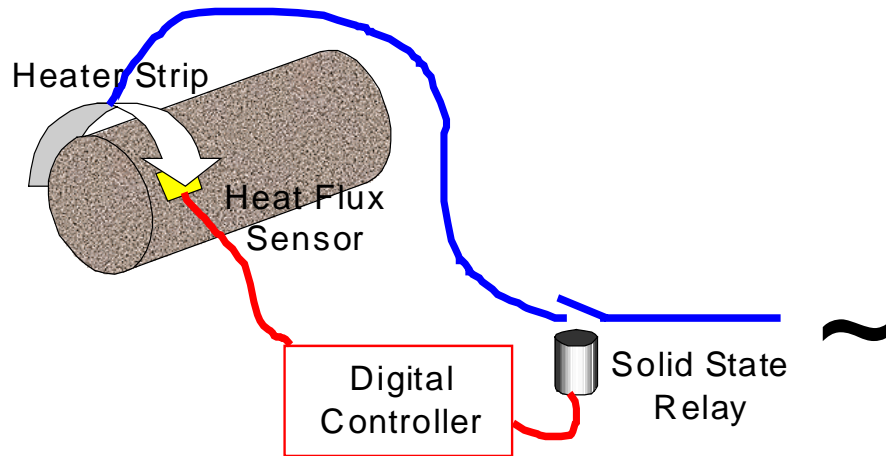
Figure 1.3: Schematic of heat guard control.

1.3 HEAT GUARD SYSTEM

The heat guard system is shown schematically in Figure 1.3. At integer multiples of a time step, currently 1 minute, the system checks the heat flux. If the heat flux out of the core at a point is outside the tolerance range (5 W/m^2), the duty cycle for the heater at that point is increased by a given increment (5%). If the heat flux is into the core, the duty cycle is decreased. Duty cycle will be a percentage between 0 and 100, ideally near 50. The duty cycle is then applied to a solid-state relay. The relay switches the heater on and off, with a 3-second base cycle, so that the heater is active for a percentage of the

3

time equal to the duty cycle percentage.

1.4 FUTURE RESEARCH

This project intends to develop into investigation of the steam-water relative permeability relationship in geothermal rocks. Due to the extremely low permeability of such rock, concerns arise regarding the time required to run the experiment, especially if a number of separate trials are required as in the original experimental method. The time scale of the experiment means that even very small heat fluxes may be significant in causing phase-change within the core; therefore, a more suitable first experiment may be nitrogen/water relative permeability at less than boiling temperatures. We have some understanding of how nitrogen/water relative permeability relates to steam/water relative permeability in porous media, and this might prove useful in simplifying our experiments on geothermal rocks.

2. BOILING HEAT CONVECTION IN A FRACTURE

This project is being conducted by Research Assistant Robb Barnitt and Professor Roland Horne. The goal is to investigate and compare the heat flux and temperature gradients that develop during boiling with liquid injection into a simulated rock fracture. Ultimately, this project aims to develop a boiling convection coefficient for use in calculating heat transfer with boiling in fractured geothermal rock. Improved understanding and modeling of heat transfer in a fracture will lead ultimately to better strategies for injection into fractured geothermal reservoirs.

2.1 INTRODUCTION

Work conducted this quarter included a third run of the aluminum disk experiment. This experiment was run again due to conflicting data trends between the first (1/99) and most recent (12/99) aluminum disk experiments. Additional work involved preparing a disk of graywacke to fit the experimental apparatus. The next experiment will utilize this rock, obtained from a Geysers core.

2.2 ALUMINUM DISK EXPERIMENT RERUN

2.2.1 Experimental Conditions

The experimental procedure employed in the repeat of this experiment was nearly identical to the original method, with a few exceptions. Data were collected with the outer edge of the apparatus exposed to atmospheric pressure. The fracture was oriented horizontally and a small positive displacement pump was used to pump water through a copper coil immersed in boiling water to provide fluid near saturated temperature. The pump was adjusted to supply discrete rates of 15, 30, and 45 ml/min, and the fracture aperture was fixed at 0.508 mm. With liquid water these rates are well within the range of laminar flow. With boiling, however, the velocity was further increased as liquid flashed to vapor in the fracture. Eight 1.0 mm diameter T-type thermocouples installed previously in the aluminum disk at varying distances from the fracture surface, recorded the temperature gradients that develop as water flashes to steam in the fracture. Calculation of the boiling convection coefficient requires that the surface temperature (T_{surf}), on the top of the aluminum disk and in the fracture, be known. This was calculated previously by linear interpolation of the linear temperature gradient which developed axially in the aluminum disk. To achieve a tangible value of T_{surf}, thin 12.5 micron thick cementable thermocouples were utilized as in the previous experiment.

The principal addition to this most recent (2/00) aluminum experiment was the use of multiple power inputs from the heater. The intent of multiple power inputs was to produce several measurements of the excess temperature (T_e) at different values of heat flux q''. These data could be compared to the established boiling curve for pool boiling conditions, and infer differences related to a confined boiling regime. Four power inputs (240, 285, 350, and 480 Watts) were supplied by the heater and were maintained at those levels for each of the three prescribed flow rates. Once steady state conditions were achieved, data was collected.

2.2.2 Experimental Results

As in the previous aluminum experiment, both the heat flux sensors and cementable surface thermocouples failed to provide reliable data. Therefore, as was done previously, values of q'' and T_{surf} were calculated using Fourier's Law of heat conduction and the assumed thermal conductivity of the aluminum. In general, these results are more reliable than those obtained previously. However, as shall be clear in the following graphs, the data point collected at 240 W and 45 ml/min is anomolous.

Using the values for q'' and T_e, a boiling convection coefficient h can be determined for each flow rate.

$$h = q'' / T_e$$

$$[W / m^2 K] \equiv [(W / m^2) / (K)]$$

The results obtained for this third (2/00) aluminum experiment are presented in Table 2.1.

Table 2.1: Results of 2/00 aluminum experiment.

Power (W)	Flow Rate (ml/min)	T_{surf} (ºC)	T_{sat} (ºC)	T_e (ºC)	$q'' =$ (W/m²)	$h =$ (W/m²K)
240	15	102.35	99.91	2.44	38,855	15,897
240	30	101.54	99.27	2.27	38,535	16,983
240	45	100.42	95.59	4.83	38,140	7,894
285	15	103.34	99.81	3.53	46,888	13,276
285	30	102.65	99.07	3.58	48,496	13,564
285	45	101.67	97.43	4.24	47,671	11,244
350	15	105.02	100.28	4.74	61,656	13,011
350	30	104.03	99.29	4.74	59,405	12,543
350	45	103.03	98.63	4.40	60,202	13,686
480	15	110.20	100.93	9.27	102,756	11,084
480	30	107.94	99.82	8.12	102,548	12,635
480	45	107.07	99.38	7.69	98,899	12,862

In Figures 2.1 through 2.3, heat flux, excess temperature, and boiling convection coefficient data are graphed for each of the four power inputs. The anomolous point at 240 W and 45 ml/min affects the graphical presentation of T_e and h.
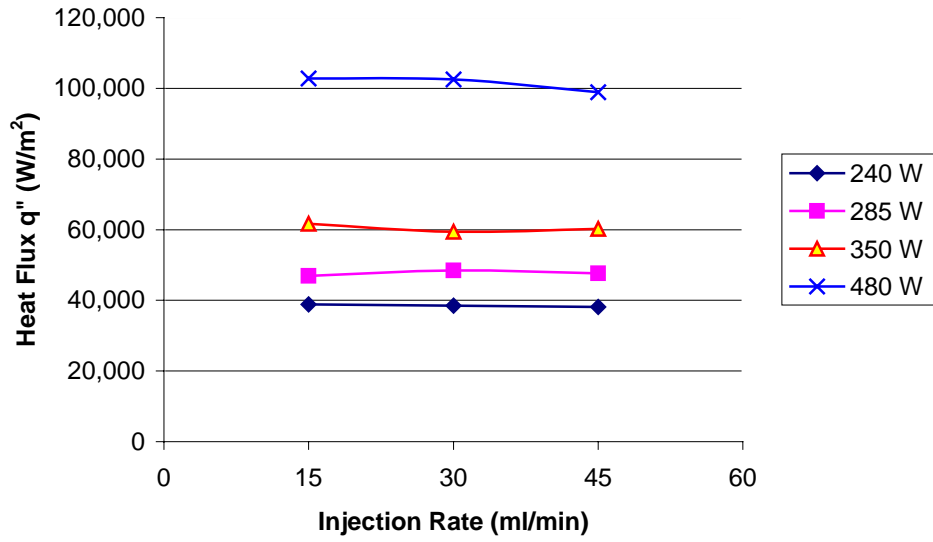
Figure 2.1: Heat flux variance with power and flow rate.

It is clear from Figure 2.1 that heat flux is not a function of flow rate on a non-porous surface.
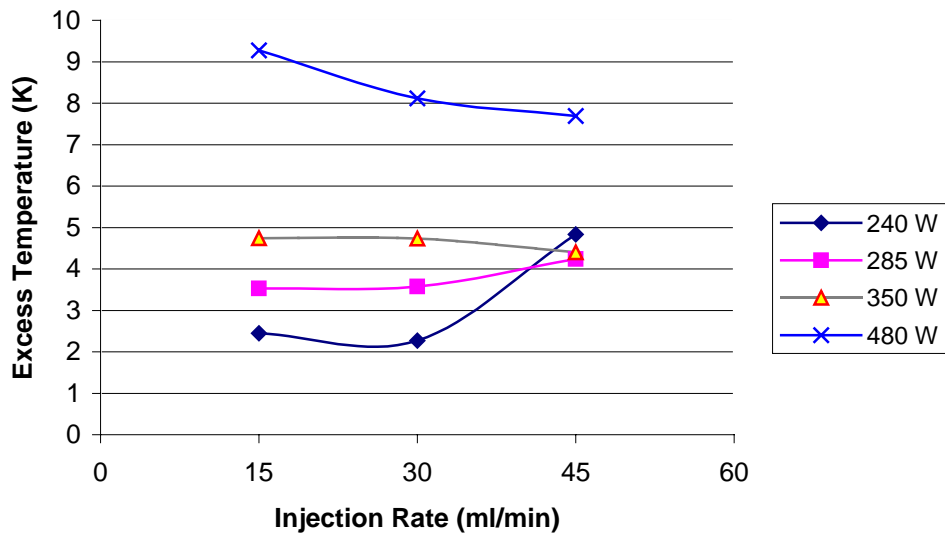

Figure 2.2: Excess temperature variance with power and flow rate.

Essentially no trends are apparent in Figure 2.2, indicating that T_e is not a function of flow rate on a nonporous surface.
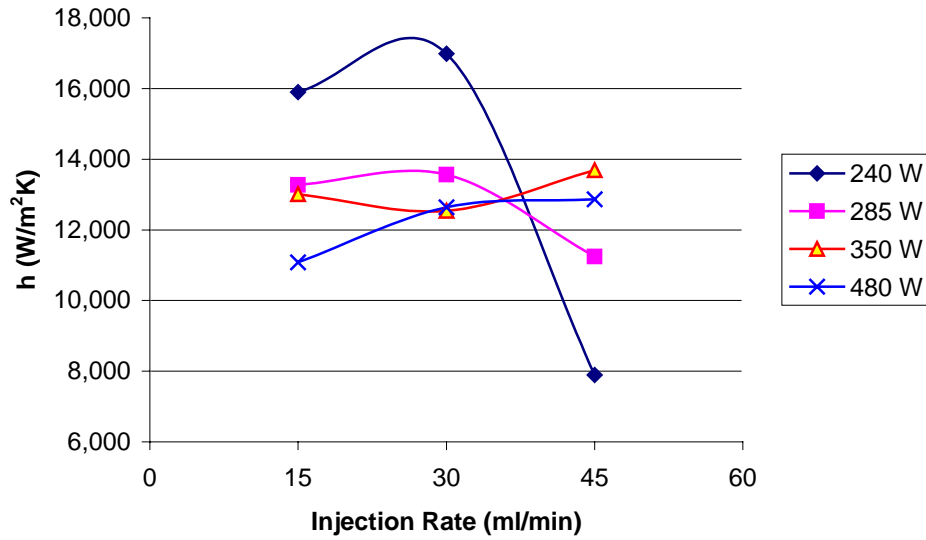
Figure 2.3: Boiling convection coefficient variance with power and flow rate.

Essentially no trends are apparent in Figure 2.3, indicating that *h* is not a function of flow rate on a non-porous surface.

For a nonporous surface, it appears the q'', T_e, and *h* values are not coupled to the injection rate. This contrasts results obtained for the porous sandstone, for which it was observed that q'' decreases, T_e increases, and *h* decreases with increasing injection rate. This phenomena should be clarified following evaluation of the upcoming graywacke experiment.

Comparison of the pool boiling curve to data generated during this experiment was not possible because of the relatively low values of T_e. A T_e of around 30 K, rather than the experimental maximum of about 10 K, would have provided data for comparison. The maximum wattage of 480 W was the maximum capability of the heater used the experiment. A more powerful heater would be required to obtain higher values of T_e.

2.3 GRAYWACKE DISK PREPARATION

The drilling of thermocouple holes was been achieved using several special drill bits. These diamond-tipped drill bits were necessary due to the extreme hardness of the graywacke matrix. However, due to this hardness, each of the three bits were destroyed during the drilling process. In several of the holes, the appropriate depth was not achieved. This discrepancy does not exceed 2 mm, and is therefore not considered significant.

2.4 FUTURE WORK

The graywacke experiment will be completed using several power inputs as done with the recent aluminum experiment. The data will be compared to that collected for non-porous and impermeable aluminum, and highly porous and permeable sandstone.

3. INFERRING ENDPOINT AND IN-SITU WATER SATURATION FROM LABORATORY AND FIELD MEASUREMENTS

This project is being conducted by Research Assistant Rodolfo Belen Jr., Research Associate Kewen Li, and Prof. Roland Horne. The aim is to infer the endpoint saturation of steam and liquid water relative permeability curves of geothermal reservoir rocks as well as the in-situ water saturation of geothermal reservoirs from laboratory and field measurements.

3.1 INTRODUCTION

Relative permeability is important in describing the flow of two-phase steam and water in geothermal reservoirs. Presently, however, relative permeability relations for steam and liquid water are not completely understood. Permeability relations are normally adopted from field data or from flow experiments in higher permeability rocks.

The experimental determination of steam and liquid water relative permeabilities is a central target of the Stanford Geothermal Program. Flow-through experiments on Berea sandstones were performed by Ambusso (1996), Satik (1998) and Mahiya (1999) utilizing X-ray computer tomography to determine steam saturation profiles. In a different approach, numerical simulation was used by Guerrero et al. (1998) to infer relative permeabilities of Berea sandstones, based on temperature, pressure, and steam saturation data obtained from steady state boiling experiments performed by Satik (1997).

All of these earlier studies used Berea sandstone in order to capitalize on its higher permeability relative to geothermal rocks, which enabled the experiments to be performed in reasonable time. This study aims to extend the understanding to low permeability geothermal rocks by determining only the endpoint saturations of the relative permeability curves. The endpoint or irreducible or immobile saturation of a certain phase is the saturation at which that phase becomes mobile in multiphase flow.

Combining information about the endpoint saturations from the "slow" geothermal rock experiments with information about the general shape of the relative permeability curves from the "faster" sandstone rock experiments will completely define the steam-liquid water relative permeability behavior.

Furthermore, determination of the endpoint and in-situ water saturation will provide a better understanding of the adsorption characteristics and fluid storage capacities of geothermal rocks. This will be valuable in estimating the size of the available resource in vapor-dominated reservoirs as well as liquid-dominated reservoirs that are experiencing dry out as a result of exploitation.

The objective of this study is to determine the endpoint saturation of the steam and liquid water relative permeability curves by inference from pressure, temperature and saturation data obtained from previous boiling experiments conducted in Berea sandstone cores. Furthermore, this study aims to determine the feasibility of performing the boiling experiments using Geysers geothermal rocks.

This study also aims to develop a model that will allow inference of the in-situ water saturation and, if possible, the endpoint water saturation from field measurements of temperature and production enthalpy. A final objective of this study is to determine the feasibility of performing flash experiments using Berea sandstone and Geysers geothermal cores to experimentally determine the endpoint water saturation as well as to confirm the field techniques.

3.2   INFERRING ENDPOINT WATER SATURATION FROM BOILING EXPERIMENTS

Results of previous steady-state boiling experiments performed by Satik (1997) were analyzed to investigate whether endpoint saturations can be inferred from the experimental data.

3.2.1 Experimental Design of Boiling Experiments Using Berea Sandstone Cores

In 1996 and 1997, Satik performed a series of boiling experiments using Berea sandstone cores. The objective of the study was to further the understanding of the boiling process in porous media and ultimately to obtain capillary functions and relative permeability relations for steam and liquid water. The steady-state boiling experiments involved the heating of a rock saturated with liquid water and observing the boiling process by continuous measurement of pressure, temperature, heat flux and steam saturation within the rock. The X-ray CT scanner was used to visualize the boiling process and to determine the three-dimensional fluid distributions within the rock. The experimental apparatus (Figure 3.1) and procedure were described in detail in the Spring 1999 quarterly report.

The boiling experiments are analogous to drainage experiments in oil and water systems, in which oil, the nonwetting fluid, is injected into a rock saturated with water, the wetting fluid, to displace the water from the rock. However, in this case, steam produced by heating the water-saturated rock displaces the liquid water from the rock.
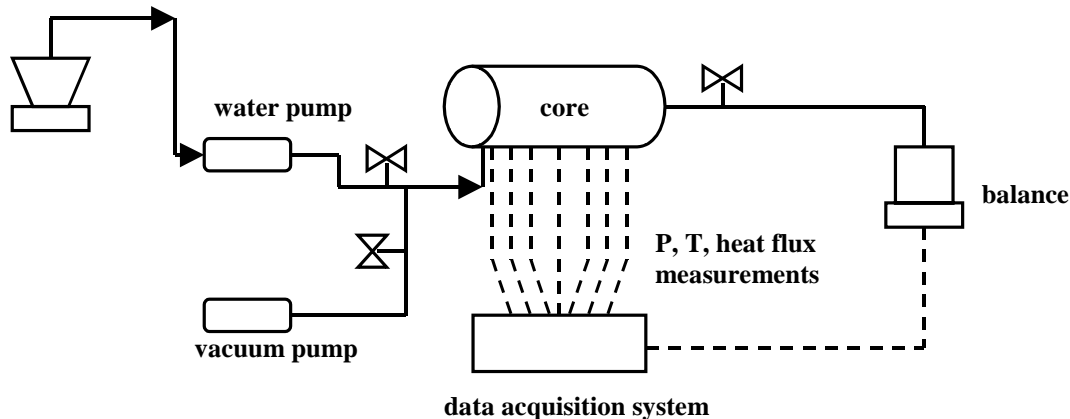
Figure 3.1: Configuration of boiling experiments.

11

3.2.2 Results of Boiling Experiments

It was observed that as the heating rate was increased, the steady state steam saturation profile indicated a progressive boiling process with the formation of distinct regions of steam, two-phase and liquid water. Figure 3.2 shows the steam saturation profile of a vertical boiling experiment performed by Satik (1997) showing the formation of steam, two-phase and liquid regions within the core as the heating rate is increased. The sudden drop in the steam saturation near the heater end of the core that marks the transition from steam to two-phase conditions is designated here as the *elbow* in the saturation profile.
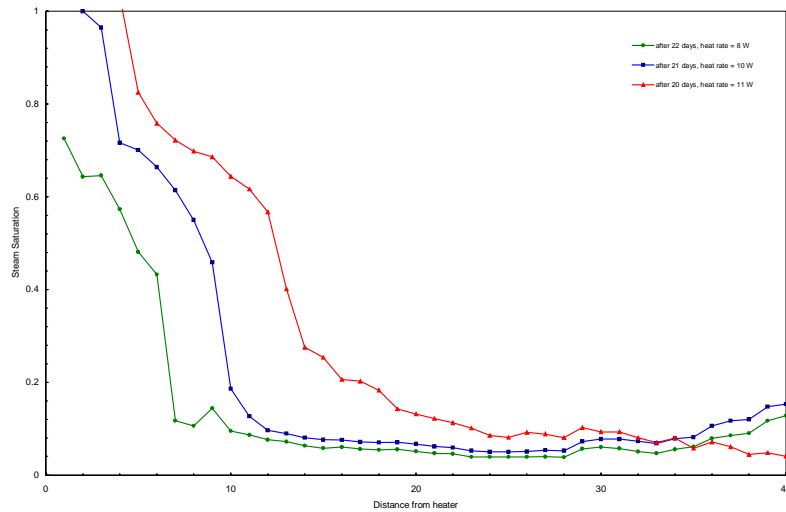

Figure 3.2: Steam saturation profile of vertical boiling experiment (Satik, Spring 1997).

### 3.2.3 Sensitivity Analysis of Boiling Experiments

It is hypothesized that the irreducible water saturation can be correlated with the elbow observed in the steam saturation profile. Analyzing the sensitivity of the boiling process to the irreducible water saturation through numerical modeling was used to test the validity of this hypothesis. The boiling process was simulated using different values of the endpoint water saturation of the relative permeability curves.   The pressure, temperature and saturation profiles were computed to verify if the elbow in the saturation profiles could be correlated with the irreducible water saturation.

In 1998, Guerrero et al. developed a two-dimensional radial iTOUGH2 model to infer relative permeability relations from the results of the boiling experiments. The same model was used in the sensitivity analysis but the grids were refined to give a better resolution of the variations in the steam saturation near the heater end of the core.

Forward calculations in iTOUGH2 were performed to predict the pressure, temperature, and steam saturation profiles along the core. It is assumed that linear steam-liquid water relative permeability functions and Leverett capillary functions govern the flow of two-phase steam in the sandstone core.

12

The nonadiabatic boiling process was simulated using varying heating rates as illustrated in Figure 3.3 and using three different values of endpoint water saturation: 0.1, 0.2, and 0.5. Steam saturation was then plotted at 0.2-cm. intervals and up to a distance 5 cm. away from the heater end. The profiles at various times are shown in Figures 3.4 to 3.6.

It is evident from the plots that the steam and two-phase regions expand as the heating rate is increased and as time progresses. As the heating rate is increased, boiling commences and steam and two-phase regions form.
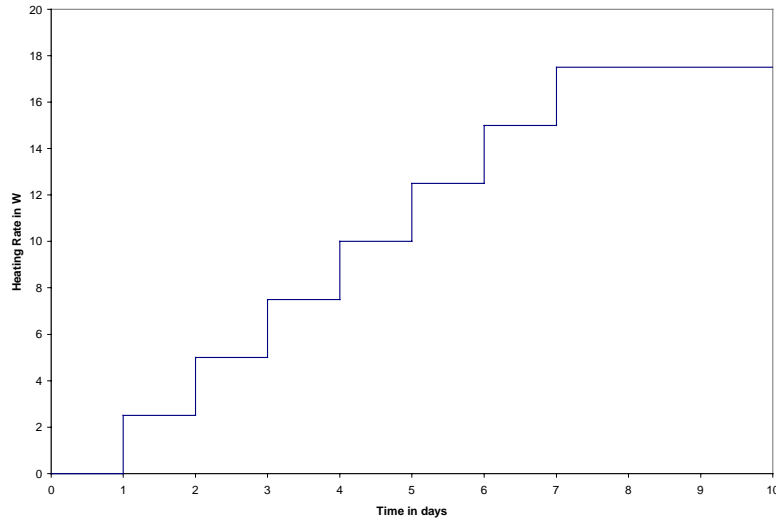
Figure 3.3: Variable heating rate profile.
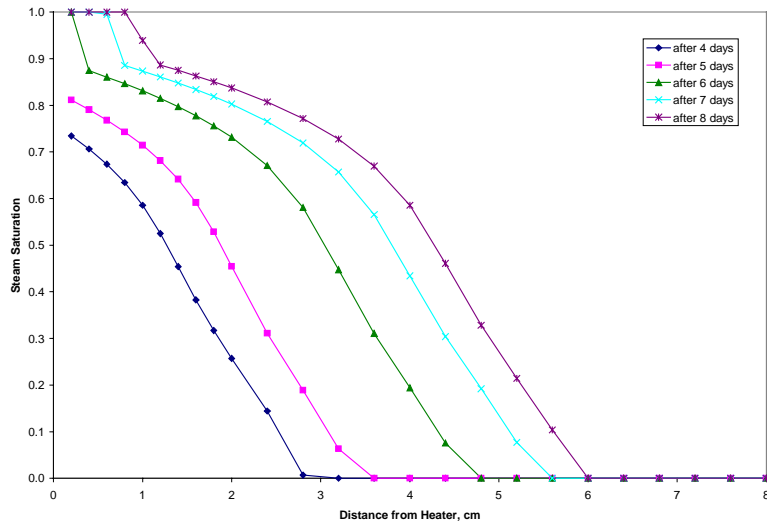
Figure 3.4: Steam saturation profile: endpoint water saturation = 0.1.

13
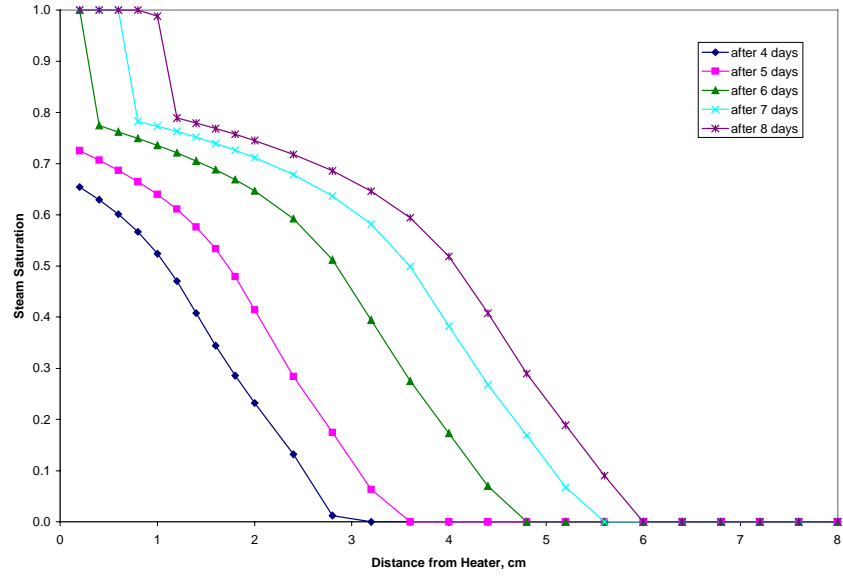
Figure 3.5: Steam saturation profile: endpoint water saturation = 0.2.
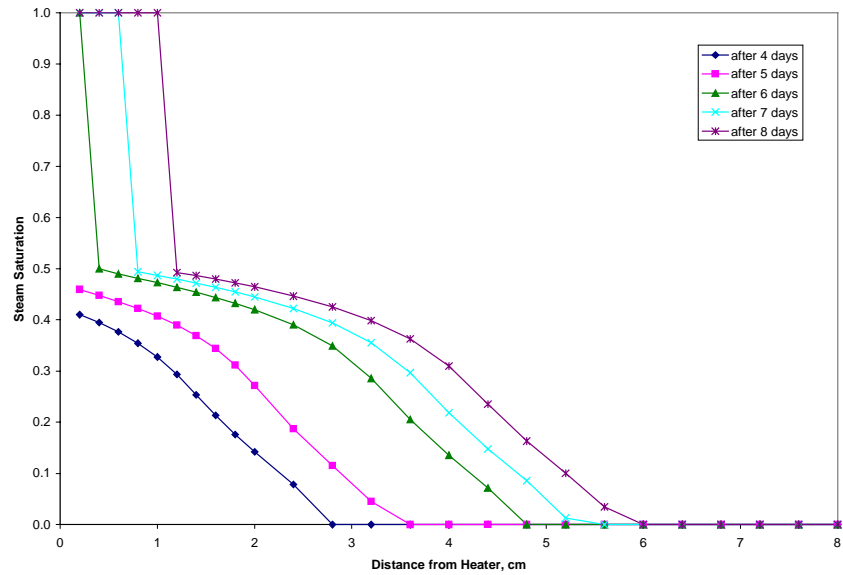
Figure 3.6: Steam saturation profile: endpoint water saturation = 0.5.

The simulation results indicate a correlation between the elbow in the steam saturation profile and the endpoint water saturation. In all three cases, the steam region extends to a distance one centimeter from the heater end. An abrupt drop in the steam saturation to a value close to the assumed endpoint water saturation marks the transition to two-phase conditions. This drop in steam saturation corresponds to the elbow in the profile. The steam saturation stays close to this value behind the elbow and then goes down further with distance from the heater end.

It is important to note that steady-state conditions were reached after about ten days of heating the core. Steady state means that the simulated steam saturation, pressure and temperature profiles remain invariant with time. As a consequence, the simulated steam saturation profiles indicate steam conditions in the region starting from the heater end to a distance one centimeter away. Beyond this region, the simulated steam saturation profiles indicate two-phase and liquid conditions.

3.2.4 Inferred Endpoint Water Saturation of Berea Sandstone Cores

Figures 3.2, and 3.7 to 3.9 show the steam saturation profiles obtained from the boiling experiments that were conducted by Satik in Spring and Summer 1997. The figures show the steam saturation profile with distance along the core and as a function of the heating rate. It is important to note that steam saturation, pressure and temperature were measured only at 1-cm intervals along the core.

It can be inferred from the experimental results that the irreducible water saturation of Berea sandstone is between 0.25 and 0.30. This inference is consistent with the experimental results reported by Mahiya in 1999 in his relative permeability experiments using Berea sandstone cores.
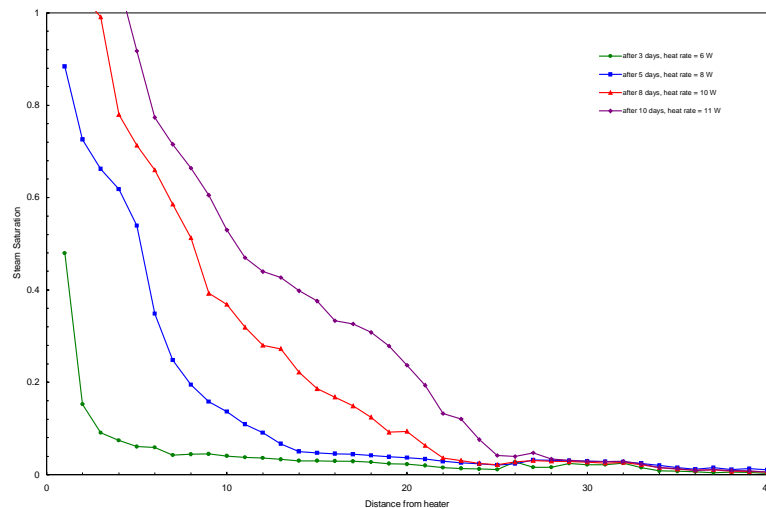
Figure 3.7: Steam saturation profile of horizontal boiling experiment
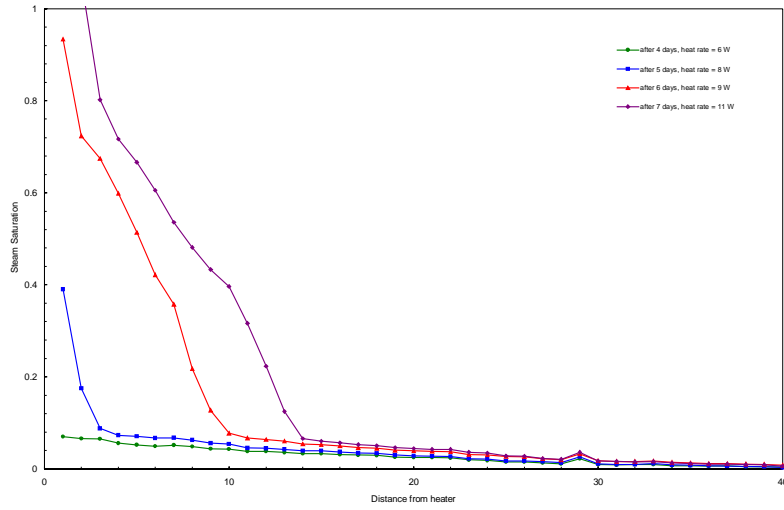
(Satik, Summer 1997).

Figure 3.8: Steam saturation profile of top-heating vertical boiling experiment (Satik, Summer 1997).
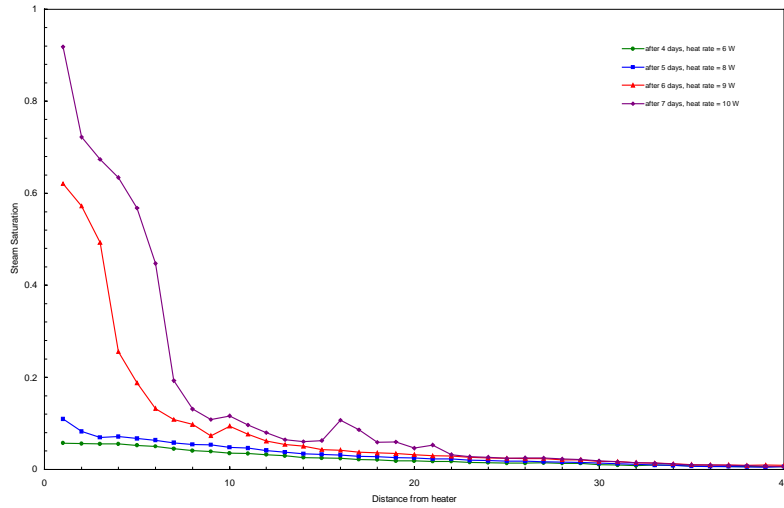
Figure 3.9: Steam saturation profile of bottom-heating vertical boiling experiment (Satik, Summer 1997).

3.2.5 Modeling Results of Boiling Experiments Using Geysers Geothermal Rocks

The boiling experiments were then modeled using Geysers geothermal rocks. The properties of the geothermal rocks used in the simulation runs are tabulated in Table 3.1.

As previously done in the Berea sandstone case, the nonadiabatic boiling process was simulated using constant and variable heating rates. Figures 3.10 and 3.11 show the

16

steam saturation profiles with distance and heating rate. The plots correspond to the profiles after one day of continuously heating the core.

Table 3.1: Geysers geothermal rock properties.

| Porosity	5%
Permeability	1×10^{-13} m^2
Rock density	2600 kg/m^3
Rock specific heat	485 J/kg°C
Rock heat conductivity	2.43 W/m°C

It is evident from the simulation results that the steam and two-phase regions expand as the heating rate is increased. However, it is important to note that in the case of the lower-porosity and lower-permeability geothermal rocks, the two-phase region is much shorter and the boiling front is much sharper relative to the Berea sandstone case, the results of which were reported in the Spring 1999 quarterly report. Consequently, the elbow in the steam saturation profile is less conspicuous in the Geysers case.
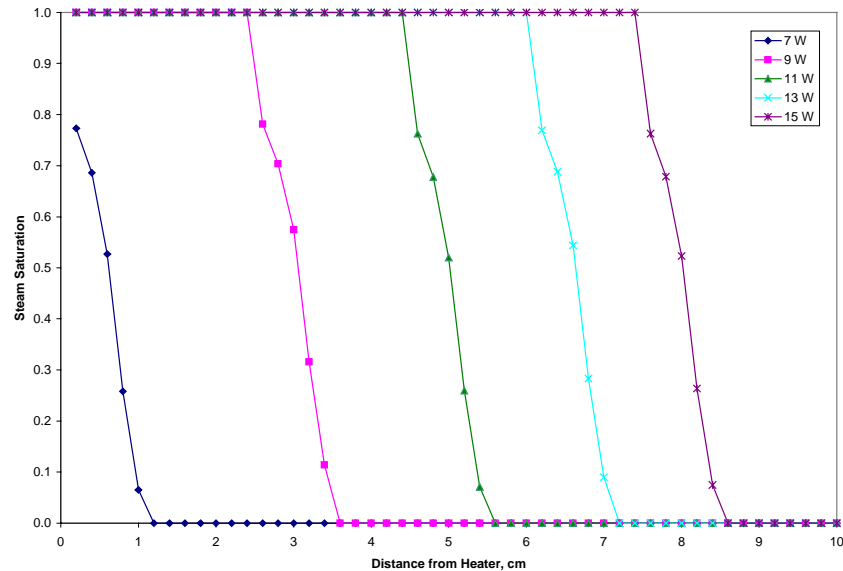
Figure 3.10: Steam saturation profiles with distance and constant heating rate, endpoint water saturation = 0.2.

Figures 3.12 to 3.14 show the simulation results when variable heating rates were used. The same heating rate profile was used in the modeling, which is shown in Figure 3.3. Likewise, steam and two-phase regions form and expand as the boiling process progresses. As expected, the two-phase region covers only a shorter distance and the boiling front is sharper. As a result, it is difficult to identify an elbow in the steam saturation profile. This very important simulation result must be taken into consideration in planning and designing boiling experiments in tighter and less permeable geothermal

17

reservoir rocks. The difficulty in identifying the elbow in the steam saturation profile may limit the usefulness of this approach in determining the endpoint water saturation of geothermal rocks from laboratory data obtained from boiling experiments.
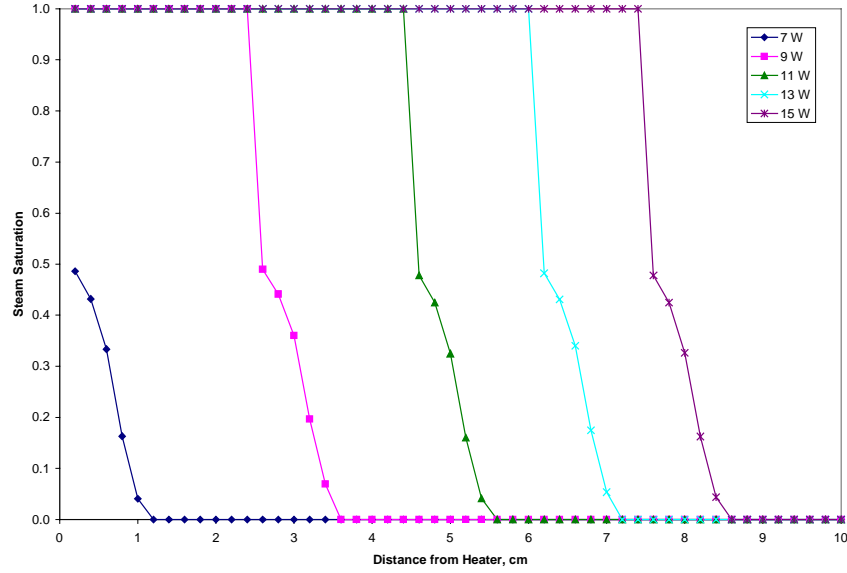
Figure 3.11: Steam saturation profiles with distance and constant heating rate, endpoint water saturation = 0.5.
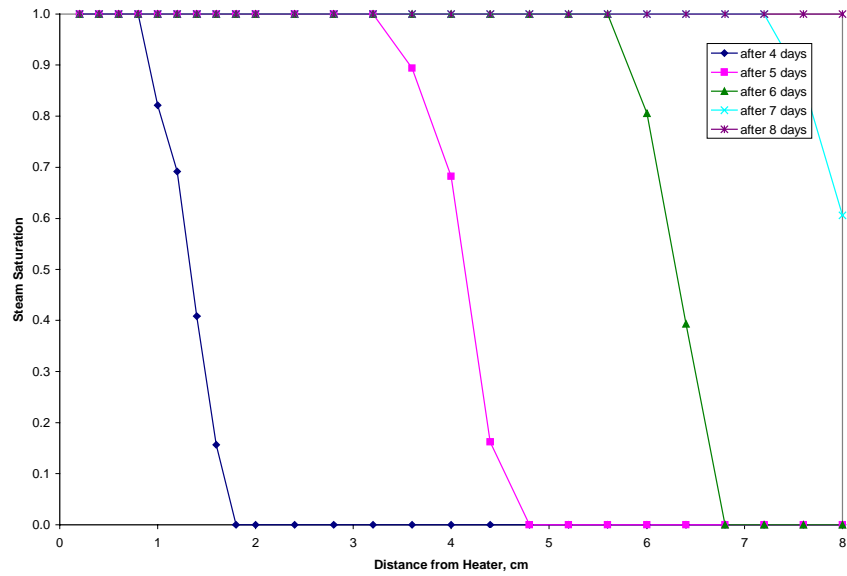
Figure 3.12: Steam saturation profiles with distance and time using variable heating rates, endpoint water saturation = 0.1.
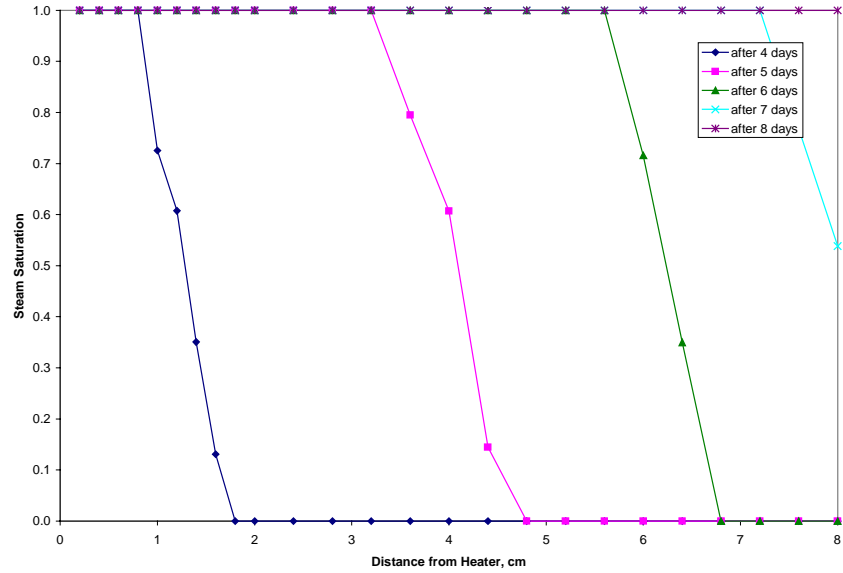
Figure 3.13:   Steam saturation profiles with distance and time using variable heating rates, endpoint water saturation = 0.2.
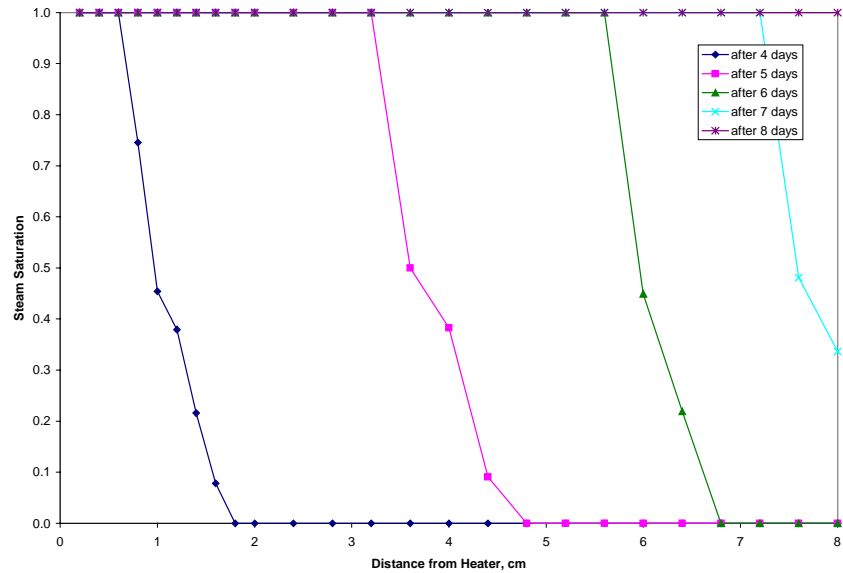
Figure 3.14:   Steam saturation profiles with distance and time using variable heating rates, endpoint water saturation = 0.5.

3.2.6 Recommendations

Based on the simulation and actual experimental results for Berea sandstone rocks, there is an apparent correlation between the endpoint water saturation and the elbow in the steam saturation profile. However, this technique may not be useful in inferring the endpoint water saturation for low porosity and low permeability geothermal rocks because of the difficulty in locating the elbow in the steam saturation profile.

19

3.3 INFERRING IN-SITU WATER SATURATION FROM FIELD MEASUREMENTS

Steam production during the exploitation of vapor-dominated geothermal reservoirs greatly exceeds what the reservoir can store as vapor. Therefore, these reservoirs must contain substantial amounts of liquid water to sustain production (James, 1968; Nathenson, 1975; Grant, 1979). In describing the response of vapor-dominated reservoirs to exploitation, it is valid to assume that the liquid water is completely immobile. Although water may be slightly mobile in the natural state of the reservoir, it is soon immobile because the water saturation drops as fluids are produced (Grant, 1979). The liquid water is adsorbed in the pores of the reservoir matrix and is able to vaporize, but is not able to flow as liquid water.

Grant (1979) estimated the in-situ water saturation of the Kawah Kamojang geothermal reservoir based on variations in the gas content of the production fluids. Changing the flow rate at the wellhead produces a response in the reservoir pressure and gas content, which allows for the estimation of the in-situ water saturation or the endpoint water saturation of the reservoir rock for this case of a vapor-dominated reservoir. In contrast, this study aims to infer the in-situ water saturation and, possibly, the endpoint saturation from field measurements of changes in the flowing enthalpies and production rates of producing wells.

Flow and lumped-parameter models can be used to describe the pressure, temperature and saturation distributions accompanying production. In the Spring 1999 quarterly report, the flow model used by Grant to infer the in-place water saturation of the Kawah Kamojang geothermal reservoir was presented.

This study aims to develop a model that will be used to infer the in-situ and endpoint water saturations using field production data. Furthermore, this study aims to extend the model to liquid-dominated reservoirs that produce two-phase steam. The aim is to extrapolate the in-situ and endpoint water saturation of the reservoir rocks using field production data.

3.3.1 Zero-Dimensional Models

Differential material and energy balance equations that describe the response of geothermal reservoirs to exploitation can be simplified to form zero-dimensional models. For the case of vapor-dominated geothermal systems, the only mobile phase is steam and the material and energy balances given by Equations 3.1 and 3.2 can be combined and simplified into Equation 3.3.

$$\phi \frac{\partial}{\partial t}\{s\rho_w + (1-s)\rho_s\} = -\nabla \cdot (u_s \rho_s) \tag{3.1}$$

$$\frac{\partial}{\partial t}\{(1-\phi)\rho_r c_r T + \phi s \rho_w h_w + \phi(1-s)\rho_s h_s\} = -\nabla \cdot (u_s \rho_s h_s) \tag{3.2}$$

$$s_o = \frac{(1-\phi)}{\phi} \frac{\rho_r c_r (T_o - T_d)}{\rho_w (h_s - h_w)\big|_{T_o}}$$
(3.3)

This zero-dimensional model allows the calculation of the in-situ water saturation using rock and fluid properties and the initial, T_o, and dry-out, T_d, downhole temperatures. In this case, the dry-out temperature is that temperature at which the reservoir has completely dried out and has started to produce superheated steam. The zero-dimensional model assumes that the steam enthalpy is invariant with pressure and temperature.

On the other hand, for the liquid-dominated reservoir case, the differential material and energy balance equations (Equations 3.4 and 3.5) and the simplified equations describing the zero-dimensional model (Equations 3.6 and 3.7) are much more complicated because both water and steam phases are mobile.

$$\phi \frac{\partial}{\partial t}\{s\rho_w + (1-s)\rho_s\} = -\nabla \cdot (u_w \rho_w + u_s \rho_s)$$
(3.4)

$$\frac{\partial}{\partial t}\{(1-\phi)\rho_r c_r T + \phi s \rho_w h_w + \phi(1-s)\rho_s h_s\} = -\nabla \cdot (u_w \rho_w h_w + u_s \rho_s h_s)$$
(3.5)

$$\phi V \Delta(s\rho_w) + \phi V \Delta\{(1-s)\rho_s\} + m_w' + m_s' = 0$$
(3.6)

$$\phi V \Delta(s\rho_w h_w) + \phi V \Delta\{(1-s)\rho_s h_s\} + (1-\phi)V\rho_r C_r \Delta T + m_w' h_w' + m_s' h_s' = 0$$
(3.7)

The zero-dimensional model assumes that the enthalpy of the produced fluids is equal to the enthalpy of the reservoir fluids at the final state.

3.3.2 TOUGH2 Two-Phase Radial Flow Model

The zero-dimensional models assume that the pressures, temperatures and saturations are uniform throughout the reservoir. These models do not take into account the transient and spatial effects of two-phase flow in the reservoir. In order to verify the validity and usefulness of these models, two-phase radial flow was modeled using TOUGH2. The TOUGH2 simulation results were then compared with those predicted by the zero-dimensional models.

A cylindrical reservoir model was used in the TOUGH2 simulation runs. A single well maintained at constant downhole wellbore pressure was placed in the middle of the reservoir. Table 3.2 summarizes the reservoir and wellbore parameters used in the simulation runs.

Table 3.2: TOUGH2 reservoir model and wellbore parameters.

Porosity	5%
Permeability	$1 \times 10^{-13} \text{ m}^2$
Rock density	2600 kg/m^3
Rock specific heat	485 J/kg°C
Reservoir radius	1000 m
Reservoir thickness	10 m
Initial reservoir temperature	280 °C
Constant downhole wellbore pressure	200 psia

Figure 3.15 to 3.17 are semilog plots of the saturation, temperature and pressure profiles with time and radial distance from the well. Initially, water saturation throughout the reservoir is 0.3. As a response to production, reservoir pressure, temperature and saturation drop and boiling near the wellbore commences. The boiling front moves farther into the reservoir away from the well as two-phase steam is produced. However, water saturation stays above and never goes below the immobile water saturation. The reservoir eventually produces dry saturated steam. During this time, reservoir saturation has dropped below the immobile water saturation. Water remaining in the reservoir during this period is immobile water, which is able to vaporize but not able to flow.

At some point during production, the reservoir completely dries out and starts to produce superheated steam. Water saturation has dropped to zero throughout the reservoir. This sequence of events is labeled in Figure 3.15.
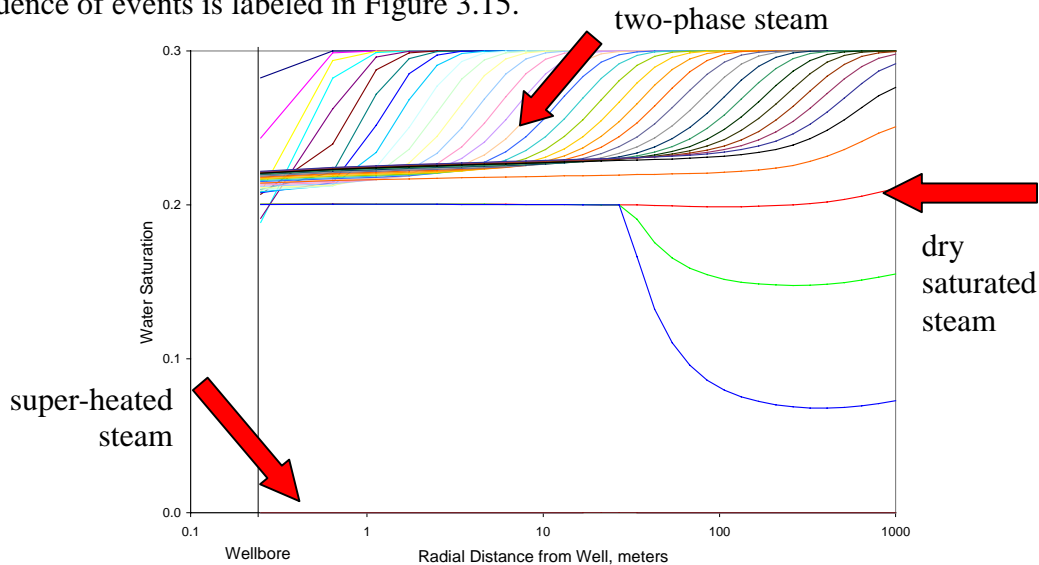
Figure 3.15: Water saturation profile with distance and time: initial water saturation = 0.3; immobile water saturation = 0.2.

22
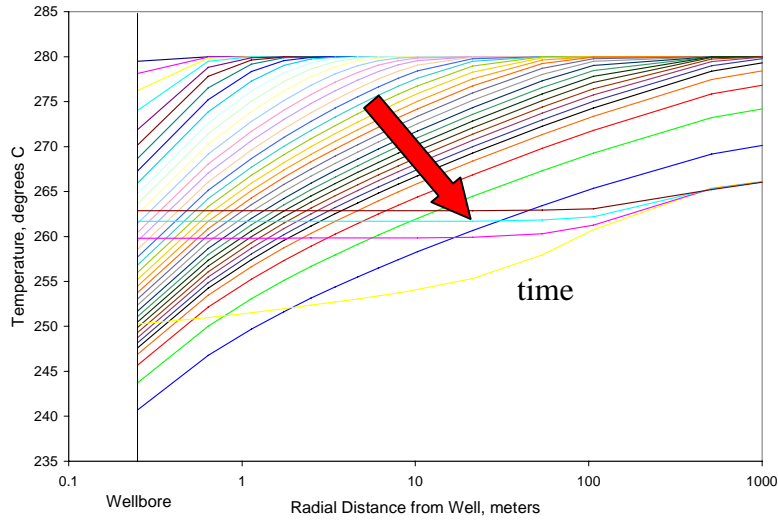
Figure 3.16: Temperature profile with distance and time: initial water saturation = 0.3; immobile water saturation = 0.2.
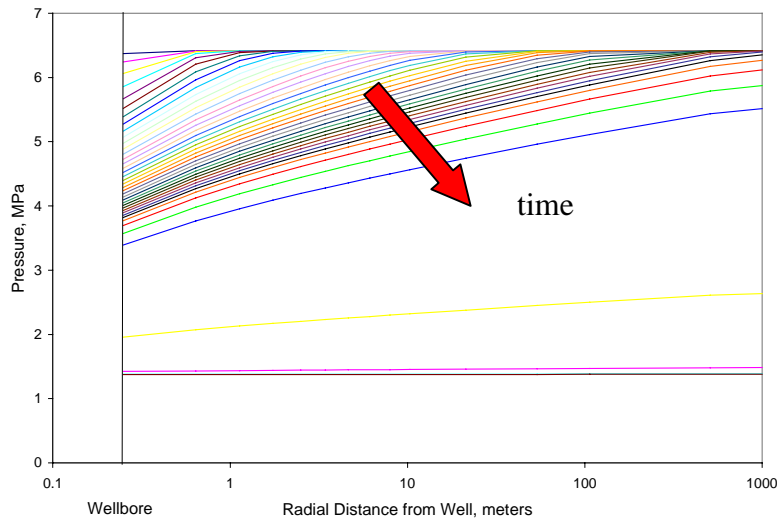
Figure 3.17: Pressure profile with distance and time: initial water saturation = 0.3; immobile water saturation = 0.2.

3.3.3 Comparison of TOUGH2 Two-Phase Radial Flow Model with Zero-Dimensional Model

Figure 3.18 compares the production enthalpies and reservoir temperatures simulated by TOUGH2 with those predicted by the zero-dimensional model for a vapor-dominated reservoir case. There appears to be a very good agreement between the simulation and the modeling results.

The simulated dry-out temperature was then used to calculate the in-situ water saturation using Equation 3.3. The zero-dimensional model gave the correct in-situ water saturation, which in this case, is equal to the endpoint or immobile water saturation. This result

23

confirms that the zero-dimensional model can be used to infer both the in-place and endpoint water saturation of vapor-dominated geothermal reservoirs by knowing the initial and dry-out reservoir temperatures. Figure 3.19 is another vapor-dominated case but with a higher in-situ water saturation equal to 0.3.

Figure 3.18: Production enthalpy and reservoir temperature profiles: vapor-dominated case; initial water saturation = 0.2; immobile water saturation = 0.2.

Figure 3.19: Production enthalpy and reservoir temperature profiles: vapor-dominated case; initial water saturation = 0.3; immobile water saturation = 0.3.

In the last two cases, reservoir temperatures simulated by TOUGH2 agreed satisfactorily with the modeled temperatures. However, reservoir temperatures are not normally measured in the field. Instead, production and downhole temperatures are routinely

24

measured in the production wells. Figure 3.20 is a plot comparing TOUGH2 simulated downhole temperatures and modeled reservoir temperatures.

Figure 3.20: Production enthalpy and production temperature profiles: vapor-dominated case; initial water saturation = 0.3; immobile water saturation = 0.3.

It is evident from Figure 3.20 that there is an initial sudden drop in the downhole wellbore temperature as a response to production. After this early transient period, downhole temperatures fall down at the same rate as the reservoir temperatures. Downhole temperatures simulated by TOUGH2 were then used to estimate the in-situ water saturation using Equation 3.3. The initial temperature, T_o, was taken to be the stable temperature after the early transient period. The zero-dimensional model still gave the correct in-situ water saturation.

Therefore, either downhole wellbore or reservoir temperatures can be used to estimate the in-place water saturation using the zero-dimensional model. However, it is important that the appropriate initial and dry-out temperatures be used in Equation 3.3.

On the other hand, the results are different for liquid-dominated geothermal reservoirs. As indicated in Figures 3.21 and 3.22, the reservoir initially produces two-phase steam. Then there is a period of dry saturated steam production when reservoir saturations have dropped below the immobile water saturation of the rocks. Eventually, the reservoir completely dries out and produces superheated steam.

During the period of dry saturated steam production, there is an apparent good agreement between the production enthalpies and temperatures simulated by TOUGH2 and predicted by the zero-dimensional model. However, there is a significantly poor match during the initial period of two-phase steam production. The zero-dimensional model greatly underestimates the production enthalpies and overestimates the temperatures. It is important to note that both TOUGH2 simulation and zero-dimensional modeling results

25

indicate the same trend in the enthalpies of the production fluids and the temperature drop in the reservoir as a result of fluid withdrawal.
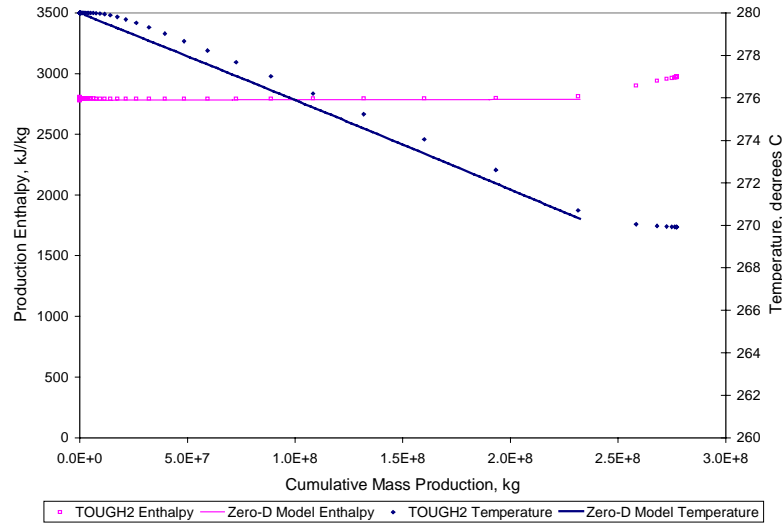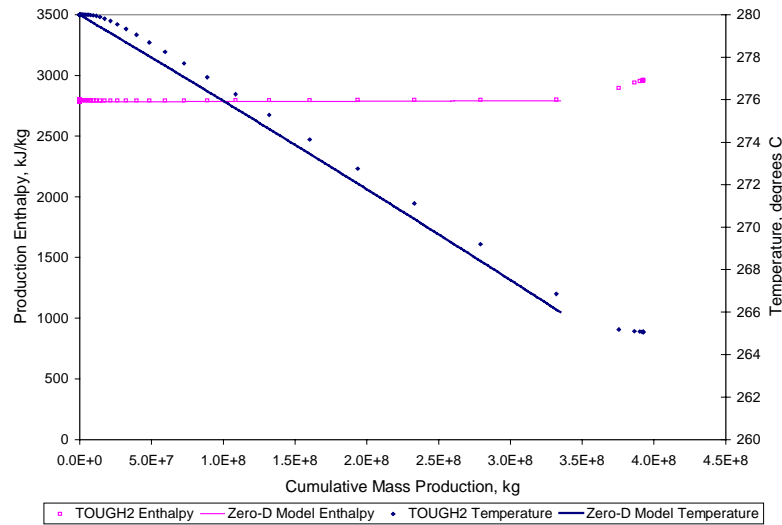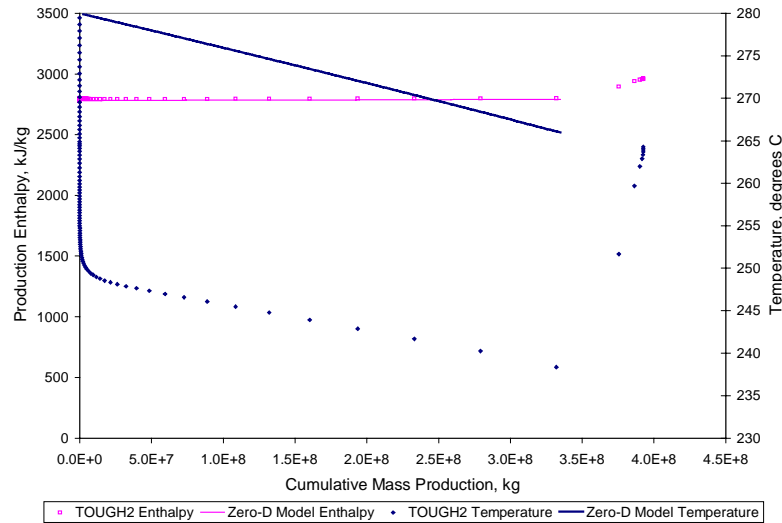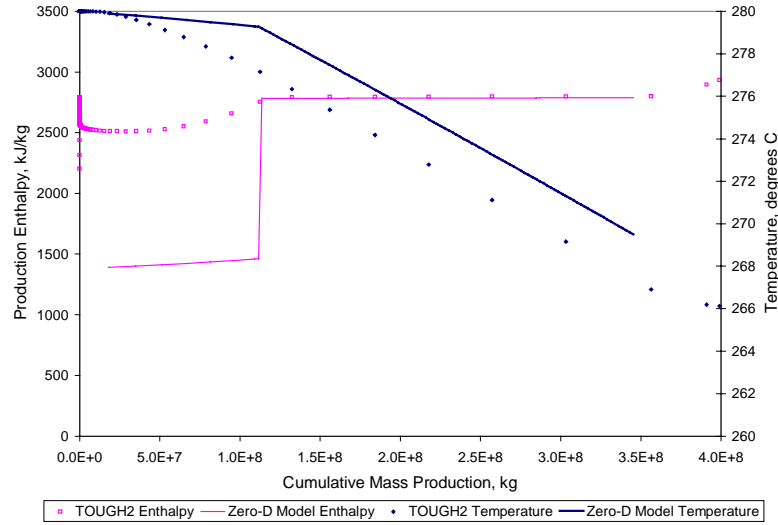

Figure 3.21: Production enthalpy and reservoir temperature profiles: liquid-dominated case; initial water saturation = 0.3; immobile water saturation = 0.2.
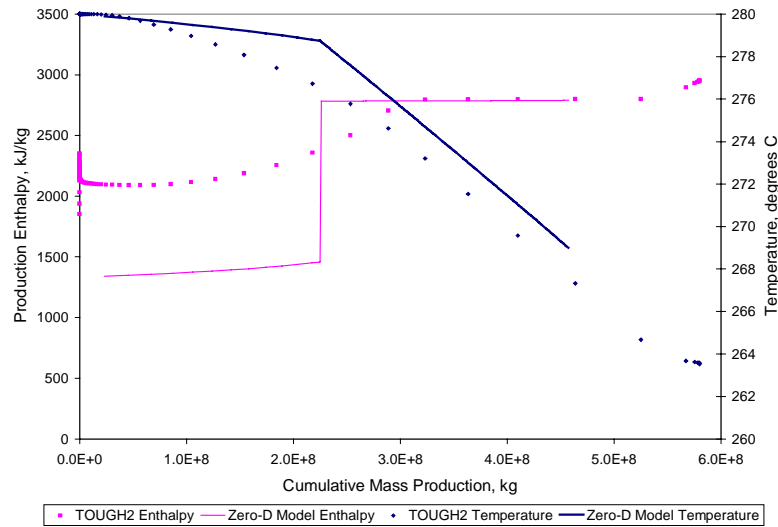
Figure 3.22: Production enthalpy and reservoir temperature profiles: liquid-dominated case; initial water saturation = 0.4; immobile water saturation = 0.2.

3.3.4 Future Work

Future work is directed towards improving the model for liquid-dominated geothermal reservoirs based on the TOUGH2 simulation results. Figure 3.23 is a plot of production enthalpy and temperature for different values of in-situ water saturation and a fixed immobile water saturation. On the other hand, Figure 3.24 is a similar plot but for different values of immobile water saturation and a fixed in-situ water saturation.

26
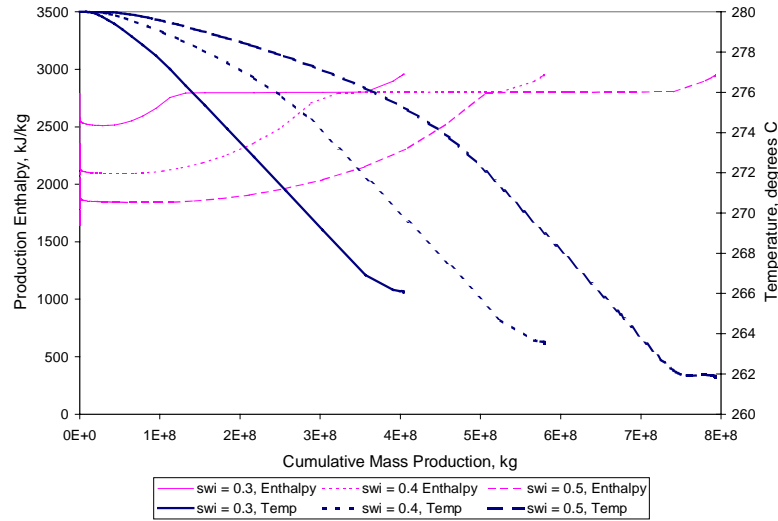
Figure 3.23:   Production enthalpy and reservoir temperature profiles: varying initial water saturation; immobile water saturation = 0.2.
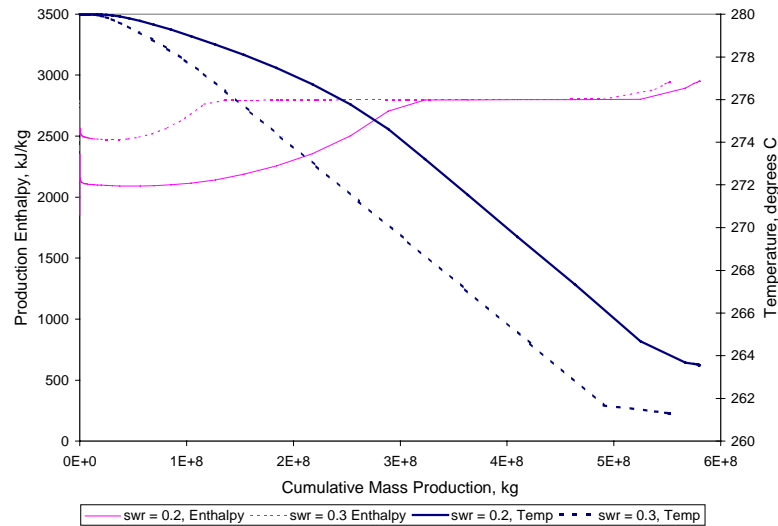
Figure 3.24:   Production enthalpy and reservoir temperature profiles: initial water saturation = 0.4; varying immobile water saturation.

There is an apparent trend in the two-phase steam enthalpies, temperatures and cumulative mass production with the mobile water saturation in the reservoir. Two-phase enthalpies are lower, temperatures are higher and cumulative mass production is greater in the case of reservoirs with higher mobile water content, which means either the in-situ water saturation is high or the immobile water saturation is low. Dry steam saturation production commences at a later time in the life of a reservoir with higher mobile water content.   These observations will be considered in improving the current model for liquid-dominated geothermal reservoirs.

3.4 INFERRING ENDPOINT WATER SATURATION FROM FLASH EXPERIMENTS

Flash experiments were modeled in TOUGH2 and were performed in the laboratory using Berea sandstone to determine if the endpoint water saturation can be inferred from experimental data as well as to confirm the field techniques discussed in the previous section of this report.

3.4.1 Experimental Design of Flash Experiments

The flash experiment basically involved depressurizing a core initially saturated with liquid water and allowing the water to flash to atmospheric pressure. The experimental apparatus was very similar to that of the boiling experiment performed by Satik, the configuration of which is shown in Figure 3.1. The set-up consisted of a core holder housing the core, a data acquisition system, a vacuum pump, a water pump, a condenser and a balance. The core was insulated with a fiber blanket to minimize heat losses. One end of the core was connected to a condenser and another water reservoir placed on a balance that was used to monitor the amount of water or condensed steam produced from the core during the flash process. A backpressure regulator attached to the outlet end was used to control pressure inside the core. Pressure and temperature were measured along the core using pressure transducers and thermocouples and were automatically recorded in a data acquisition system.

The core was first dried and then vacuumed to completely remove air trapped inside the pore spaces. The rock was then fully saturated with deaerated water, pressurized to 20 psig and heated to about 110°C using surface heaters. After pressures and temperatures along the core had stabilized, the pressure at the outlet end was quickly reduced to atmospheric pressure to initiate flashing of the liquid water. Pressures, temperatures and water production from the core were recorded continuously by the data acquisition system during the entire flash experiment.

3.4.2 Results of Flash Experiments

Figure 3.25 is a series of plots showing profiles of pressures, temperatures and corresponding saturation temperatures with time at different locations in the core. Pressures and temperatures were measured at eight different locations spaced 5 cm apart from each other along the core.   Figures 3.26 and 3.27 are plots of pressure and temperature as a function of the cumulative mass production.

The profiles show the sudden drop in temperature and pressure as soon as the core was flashed to atmospheric pressure. Furthermore, the plots indicate the advancement of the boiling front along the core as conditions stabilize with time.

3.4.3 Future Work

Future work is directed towards further analyzing the experimental results from the flash experiments as well as the TOUGH2 simulation results presented in the Fall 1999 quarterly report.
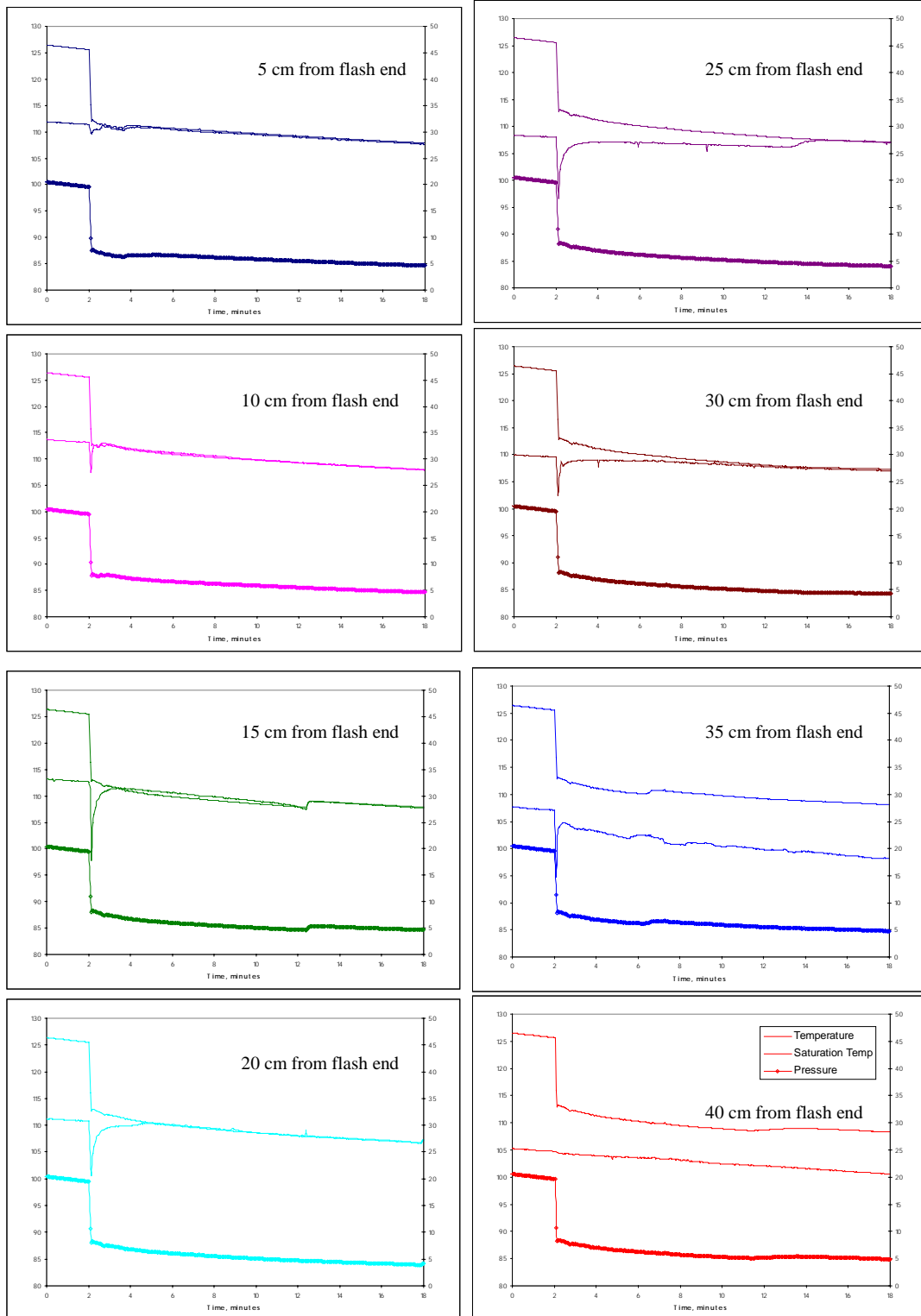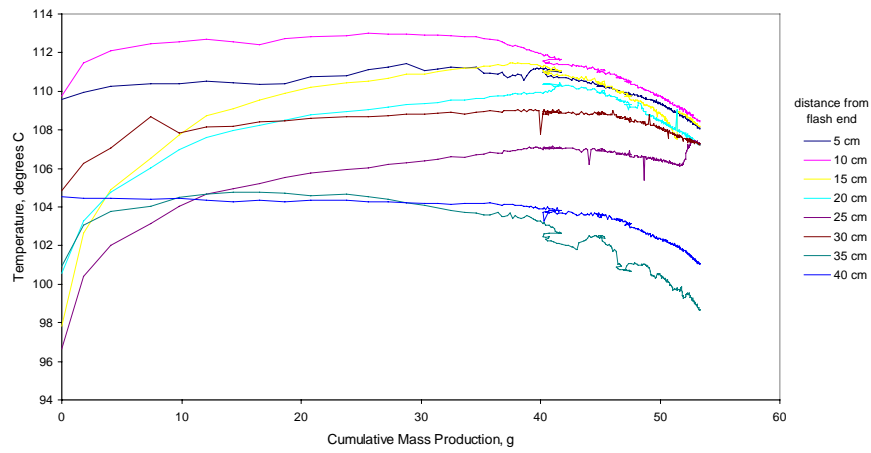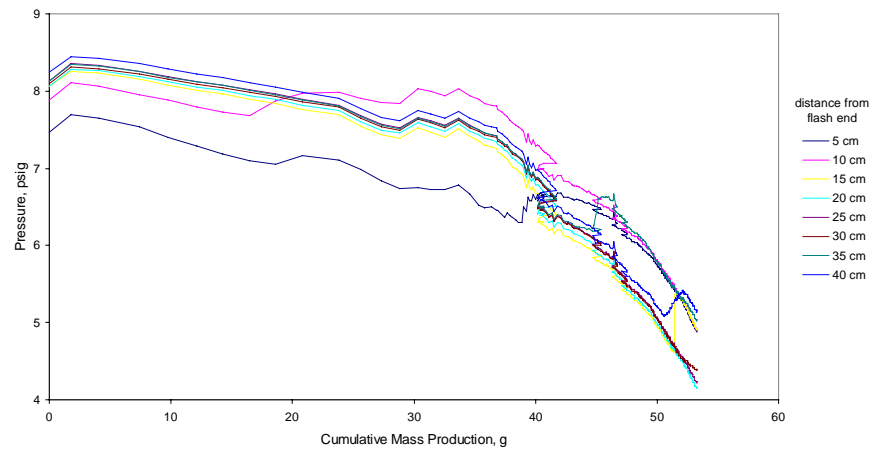
Figure 3.25: Pressures and temperatures along the core during flash experiment.

Figure 3.26: Temperature versus cumulative mass production during flash experiment.

Figure 3.27: Pressure versus cumulative mass production during flash experiment.

4. STEAM-WATER CAPILLARY PRESSURE

This research project is being conducted by Research Associate Kewen Li and Professor Roland Horne. The objective of this project is to develop a method for measuring and calculating steam-water capillary pressure in geothermal systems.

4.1 SUMMARY

We used a steady-state flow method to measure steam-water capillary pressures using an X-ray CT technique to monitor and measure the saturation and distribution of water in the core sample. The drainage steam-water capillary pressure was calculated using a formula derived from the Kelvin equation after measuring the pressures and temperatures of the water phase. The steam-water capillary pressure of the Berea sandstone sample was about 0.07 MPa (10.4 psi) at a water saturation of around 30% and a temperature of about 120°C. The steam-water capillary pressure of the Berea sandstone sample was scaled up for a rock from The Geysers field using the experimental data of steady-state flow and the results obtained were consistent with those measured by Persoff and Hulen (1996) using an adsorption method. A mathematical model to calculate steam-water capillary pressure of geothermal rocks has been developed for application in geothermal reservoir engineering and numerical simulation.

4.2 INTRODUCTION

In recent years, much attention has been paid to the measurement of steam-water relative permeability (Sanchez and Schechter, 1990, Ambusso, 1996, Satik, 1998, Mahiya, 1999, Li and Horne, 1999, and Horne et al., 2000). However, less attention has been paid to the experimental measurement of steam-water capillary pressure, even though capillary pressure is of equal significance to relative permeability and plays an important role in geothermal reservoirs. As an example, Tsypkin and Calore (1999) developed a mathematical model of steam-water phase transition with capillary forces included. They investigated the main characteristics of the vaporization process and found that capillary pressure can play a stabilizing role for the vaporization front, causing a sharp front to develop.

Urmeneta et al. (1998) also studied the role of capillary forces in the natural state of fractured geothermal reservoirs and found that capillary pressure tended to keep the vapor phase in the fractures and the liquid phase in the matrix. The numerical results from Urmeneta et al. (1998) showed that capillary forces control the transfer of fluids between fractures and matrix, the stability of the liquid-dominated two-phase zone, and the distribution of steam and water in geothermal reservoirs. Hence, the value of capillary pressure will influence the estimation of the energy reserves and production performance. Unfortunately, there are few experimental data of steam-water capillary pressure for steam-water flow in porous media.

Sta. Maria and Pingol (1996) inferred values of capillary pressure from the adsorption data of Horne et al. (1995) for rock samples from The Geysers geothermal field and found the capillary pressure to range from 0 to 586 MPa (0 to 86000 psi). Persoff and Hulen (1996) also inferred the capillary pressure from adsorption data of The Geysers

rock samples and found the capillary pressure ranging from 0 to about 190 MPa (0 to 28000 psi). Persoff and Hulen (1996) used different salt solutions to obtain a wide range of vapor pressures in the rock sample. These results show some inconsistency. Therefore, it is necessary to develop a reliable technique to measure and calculate the steam-water capillary pressure directly. We also need to develop a method to scale up the experimental data to reservoir conditions. This is of importance for geothermal reservoir engineering and numerical simulation.

The adsorption/desorption tests that have been used to infer capillary pressure are static processes in which there is no steam-water flow. In actual geothermal reservoirs, however, capillary pressure plays its important role while steam and water flow simultaneously through the rocks. Hence the process governing an adsorption test may not represent the mechanisms under actual fluid flow conditions in geothermal reservoirs. Consequently, the capillary pressures calculated using adsorption test data may or may not be the same as those measured using a dynamic method in which steam and water flow simultaneously through the porous medium. It is known that capillary pressure is influenced significantly by the contact angle. The contact angle in a static state (no fluid flow) is usually very different from the contact angle in a dynamic state (with fluid flow). Hence the capillary pressure is likely to be different under static and dynamic conditions. Finally, very strict sealing requirements have to be achieved for long periods of time during the adsorption tests, which is very difficult especially at high temperatures. These disadvantages of adsorption tests may be overcome by using a steady-state flow method for measuring steam-water capillary pressure.

In this study, a method to calculate steam-water capillary pressure has been developed using the data from steady-state steam-water flow experiments by Mahiya (1999). An X-ray CT technique was used to monitor and measure the water saturation and its distribution in the core sample. The pressures and temperatures of water phase in a Berea sandstone sample were measured at different axial positions. Water saturation was varied by changing the flow rates of steam and water at the inlet of the core sample. Experiments were conducted under near-adiabatic conditions controlled automatically by a computer. As will be described in the following sections, steam-water capillary pressures in the Berea sandstone sample can be calculated using a formula derived from the Kelvin equation together with the measured values of the pressure and temperature of the water phase. Following that, the steam-water capillary pressure of a rock sample from The Geysers field can be computed on the basis of the results from the Berea sandstone sample using the concept of a *J*-function. The values estimated here by this approach were compared to the vapor-water capillary pressures measured by Persoff and Hulen (1996) using an adsorption method.

4.3 THEORY

Using the Kelvin equation, steam-water capillary pressure can be calculated from the experimental data of liquid phase pressure, temperature, and related parameters. The procedure is described in this section.

The *relative pressure* (p_v/p_0), the ratio of vapor pressure, p_v, on a curved surface to the vapor pressure, p_0, on a flat surface, is used to characterize the capillary condensation on curved surfaces. Kelvin established the relationship between the relative pressure and the curvature of the interface along with other properties of the fluid and the substrate. In a circular capillary tube with a radius of r, the relative pressure can be calculated using the Kelvin equation as follows:

$$\ln(\frac{p_v}{p_0}) = -\frac{2\sigma M_w \cos\theta}{r\rho_w RT} \tag{4.1}$$

where p_0 is the vapor pressure when the vapor-liquid interface is flat; p_v is the vapor pressure in a capillary tube of radius r when the vapor-liquid interface is curved; σ is the interfacial tension and θ is the contact angle measured through the liquid phase; R is the gas constant, T the absolute temperature, M_w the molecular weight of liquid, and ρ_w the density of liquid.

The Kelvin equation assumes that: (1) all adsorption is due only to capillary condensation; (2) adsorbate density is equal to bulk liquid density; and (3) the validity, including the constancy of σ and the system pressure p, is unimpaired at low values of r.

The capillary pressure, P_c, in a circular capillary tube is also determined by the interface curvature, fluid and substrate properties, and can be calculated as:

$$P_c = \frac{2\sigma \cos\theta}{r} \tag{4.2}$$

Combining Equations 4.1 and 4.2:

$$P_c = \frac{\rho_w RT}{M_w}\ln(\frac{p_0}{p_v}) \tag{4.3}$$

Capillary pressure is defined as the pressure difference between vapor and liquid phases:

$$P_c = p_v - p_w \tag{4.4}$$

where p_w is the pressure of liquid phase. Substituting Equation 4.4 into 4.3:

$$p_v - p_w = \frac{\rho_w RT}{M_w}\ln(\frac{p_0}{p_v}) \tag{4.5}$$

The units used in Equation 4.5 are as follows: p_v, p_w, p_0 kPa (absolute), ρ_w (g/ml), $R = 8310$ (kPa.ml)/(°K.mole), T °K, and M_w g/mole.

In our steam-water flow experiments, we can measure p_w and T at the same time and the same location, while p_0 can be calculated according to the measured saturation temperature. Therefore, p_v, as the only unknown parameter in Equation 4.5, can be obtained by Newton iteration. The capillary pressure is then computed using Equation 4.4 once p_v is known. The solver function of Microsoft$^{\circledR}$ Excel 97 was used to solve Equation 4.5 in this work.

Note that Equation 4.2 is only correct in a capillary tube with a circular shape. On the other hand, the adsorption process in porous media is governed not only by capillary pressure but also Van der Waals attractive forces, including the dispersion forces. In addition, the electrostatic forces may play an important role. In order to apply Equation 4.5 in porous media, we need to assume also that differences of pore shape from circular can be ignored. It may be necessary to make some correction to apply Equation 4.5 in porous media, in order to meet this assumption as well as all the assumptions inherent in the Kelvin equation itself. In this work, we calculated the vapor pressure in porous media using Equation 4.5 and then calculated steam-water capillary pressure using Equation 4.4. The appropriateness of using Equation 4.5 in this way was evaluated by comparing to actual capillary measurements by earlier authors.

Once the steam-water capillary pressure in the Berea sandstone sample was available, we were able to infer the steam-water capillary pressure in geothermal rocks. The procedure is described here. Capillary pressures in rocks with different porosity and permeability may be correlated using the J-function suggested by Leverett (1941) as follows:

$$P_c = \frac{\sigma \cos \theta}{\sqrt{\dfrac{k}{\phi}}} J(S_w) \tag{4.6}$$

where k, ϕ, S_w, and $J(S_w)$ are permeability, porosity, water saturation, and J-function, respectively. Assuming that the J-function in both Berea and geothermal rock samples are the same, we can calculate the steam-water capillary pressure in geothermal rocks using the following equation:

$$P_c^G(S_w) = \frac{\sigma_G \cos \theta_G}{\sigma_B \cos \theta_B} \frac{\sqrt{\dfrac{k_B}{\phi_B}}}{\sqrt{\dfrac{k_G}{\phi_G}}} P_c^B(S_w) \tag{4.7}$$

here $P_c^G(S_w)$ and $P_c^B(S_w)$ are the steam-water capillary pressures at a water saturation of S_w in a geothermal rock sample with a permeability of k_G and a porosity of ϕ_G and in a Berea sandstone sample with a permeability of k_B and a porosity of ϕ_B, respectively. Considering that the temperatures may be different in the two systems, σ_B, the surface tension in the steam-water-Berea system, and σ_G, the surface tension in the steam-water-geothermal rock system, are introduced in Equation 4.7. Similarly, θ_G and θ_B are the

contact angles in steam-water-Berea and steam-water-geothermal rock systems, respectively. Equation 4.7 was derived by applying Equation 4.6 to each type of rock – Berea and geothermal. Since the contact angle in steam-water-geothermal rock systems is not available, we assumed in this study that the contact angles in both Berea and geothermal rock samples are the same. Furthermore, if we scale the experimental data to the same temperature, the surface tension will be the same. Therefore, Equation 4.7 would be reduced to:

$$P_c^G(S_w) = \frac{\sqrt{\dfrac{k_B}{\phi_B}}}{\sqrt{\dfrac{k_G}{\phi_G}}} P_c^B(S_w)$$

(4.8)

Based on Equation 4.8, the steam-water capillary pressure in geothermal rocks can be computed once the steam-water capillary pressure in the Berea sandstone sample, and the permeability and porosity in both Berea and geothermal rocks are known. We compared the steam-water capillary pressure calculated using Equation 4.8 for a rock from The Geysers geothermal field to the steam-water capillary pressure measured in the same rock by Persoff and Hulen (1996) using an adsorption method. Because the adsorption experiments by Persoff and Hulen (1996) were conducted at a temperature of 28.5^oC and the steady-state flow tests were conducted at a temperature of 120^oC, it is necessary to scale up the capillary pressure measured by Persoff and Hulen (1996) to the same temperature, 120^oC. This was achieved using the following equation:

$$P_c^{G,T_2}(S_w) = \frac{\sigma_{T_2}}{\sigma_{T_1}} P_c^{G,T_1}(S_w)$$

(4.9)

where $P_c^{G,T_1}(S_w)$ and $P_c^{G,T_2}(S_w)$ are the capillary pressure for the same rock at the same water saturation of S_w but at different temperatures of T_1 and T_2, respectively. σ_{T_1} and σ_{T_2} are the surface tensions at temperatures T_1 and T_2.

Usually, the *J*-function is consistent for rocks with similar depositional environment. That is, the *J*-function may be the same for rocks in similar depositional environments but with different porosity and permeability. The *J*-function for geothermal rocks may or may not be different to that of Berea sandstone since the deposition conditions are not the same. Therefore, the steam-water capillary pressure calculated using Equation 4.8 for the rock from The Geysers geothermal field may not be consistent to that measured in the same rock by Persoff and Hulen (1996) using an adsorption method.

4.4 EXPERIMENTS

The experimental details regarding the collection of the data used this study have been described in Mahiya (1999). For convenience, a brief description of the fluid flow tests is repeated here. Distilled water was used as the liquid phase and to generate steam; the

specific gravity and viscosity were 1.0 and 1.0 cp at 20°C. The steam properties at high temperatures were calculated using a steam table, based on the measured values of pressure and temperature . The surface tension of steam/water at 20°C is 72.75 dynes/cm. The core sample was a Berea sandstone fired at high temperature; its permeability and porosity were 1400 md and 24.0%; the length and diameter were 43.2 cm and 5.04 cm, respectively.

A schematic of the apparatus for the steady-state flow tests is shown in Figure 4.1. One of the challenges in this steady-state flow test was to maintain an adiabatic condition. To this end, a technique using flexible guard heaters wrapped around the coreholder was developed by Mahiya (1999). The exact amount of heat that was lost from the core-fluid system was supplied back to the system using the heaters, so that the overall heat loss would be negligible. Automation and data acquisition were realized by using the software LabView 4.1 and corresponding hardware (National Instrument Co.). Steam and water saturations were measured using a Picker^{TM} Synerview X-ray CT scanner (Model 1200 SX) with 1200 fixed detectors. The voxel dimension is 0.5 mm by 0.5 mm by 5 mm, the tube current used was 50 mA, and the energy level of the radiation was 140 keV. The acquisition time of one image is about 3 seconds while the processing time is around 40 seconds.
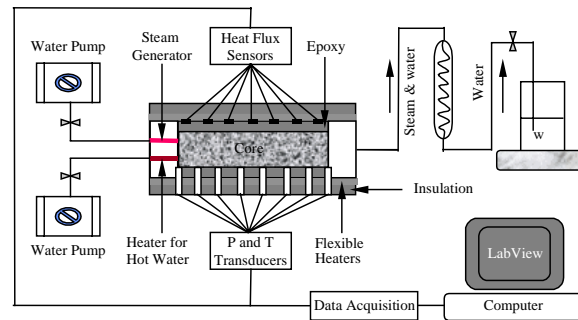
Figure 4.1: Schematic of the apparatus for steady-state flow tests.

Pressure and temperature were measured through ports at eight positions along the core spaced about 5 cm apart. The experiments used differential pressure transducers manufactured by CES Co. (Model 238) with a linearity of 0.25% full scale and a range of differential pressure from 0 to 10 psi. All the pressure transducers were calibrated before and after the experiments using a pressure gauge with an accuracy of 0.05 psi.

The core sample was dried by evacuation at about 30 millitorr while heating. Once dried, the core sample was saturated with distilled water. In order to achieve two-phase flow conditions in the core sample, dry steam and hot liquid water were injected separately from two streams at the inlet. Each stream of fluid came from deionized water pumped from a common reservoir to a boiler and then to a condensing loop. This process eliminated the dissolved air that would introduce errors in the saturation measurements. The deaerated water was then delivered to the heating head where each of the two

streams was heated to either steam or hot water (see Figure 4.1). Steam and water then became partially mixed at the interface between the core and the head, and further mixed as they entered the porous medium. Steam and water were produced from the outlet end of the core and the volumetric flow rate was computed using a balance (with an accuracy of 0.01g) and timer, and compared with the injection rates specified at the pumps. Temperatures, pressures, and saturations in the core were measured once the flow reached steady-state , and these values were used to calculate steam-water capillary pressure with Equations 4.4 and 4.5. After each set of steady-state measurements, the water saturation in the core sample was changed by adjusting the ratio of steam flow rate to water flow rate by varying the power supplied to the steam heater.

4.5 RESULTS

The steam-water capillary pressures calculated using Equations 4.4 and 4.5 with the experimental results of steady-state flow of steam and water in the Berea sandstone sample are shown in Figure 4.2. The solid line is a fitting curve using an exponential function.
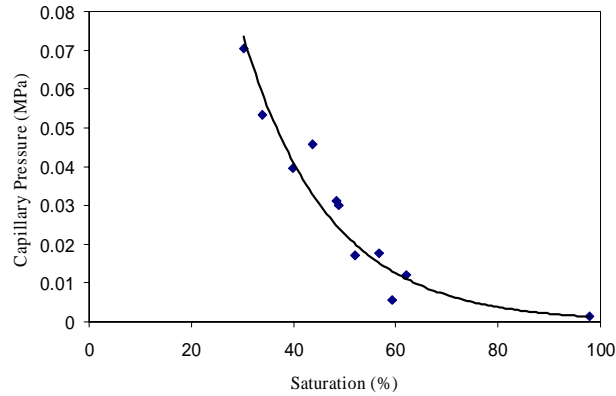
Figure 4.2: Steam-water capillary pressure curve (drainage) calculated from the data of steady-state flow of steam and water in a Berea sandstone sample.

During the experimental process, the water saturation in the Berea sandstone sample was decreased from 100 percent to the remaining water saturation, about 28 percent. Therefore, Figure 4.2 shows a drainage capillary pressure curve. The entry capillary pressure of steam is very small for this sandstone sample. The steam-water capillary pressure in the Berea sandstone sample at a water saturation of about 30% is around 0.07 MPa (10.4 psi), as shown in Figure 4.2. The water saturation remained in the core sample after the drainage by steam flooding is about 28%. The actual residual water saturation may be less than this value because of practical experimental limitations such as limited steam flooding time. However, the real residual water saturation in the core sample may be estimated using a regression analysis for the relationship between steam-water capillary pressures and water saturations.

As mentioned before, we can use Equation 4.8 to calculate the steam-water capillary pressure in geothermal rocks once the steam-water capillary pressure in a Berea

sandstone sample is available. The purpose is to compare the results with those measured by Persoff and Hulen (1996) and hence evaluate the appropriateness of the assumptions of Equation 4.8. First of all, we need to know the porosity and permeability of the geothermal rocks. Persoff and Hulen (1996) measured the porosity and permeability of four rocks from The Geysers geothermal field, the porosity ranging from 0.2% to 0.5% and the permeability ranging from 1.3 to 26 nd (10^{-6} md). The steam-water capillary pressure data were computed using Equation 4.8 for the two rock samples with the low and high limit values of porosity and permeability. Figure 4.3 shows the calculated capillary pressure curves.
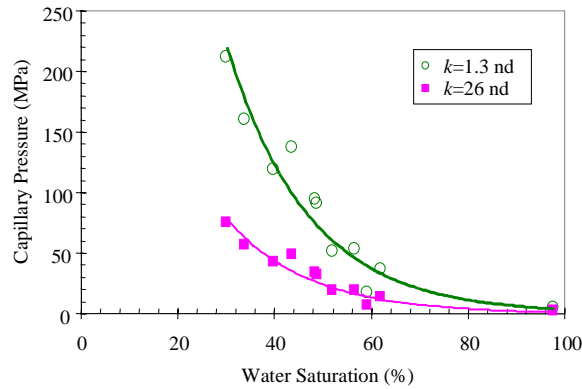
Figure 4.3: Steam-water capillary pressure curves calculated using a scaling method for two rocks from The Geysers field.

The effect of permeability on steam-water capillary pressure is significant for the geothermal rocks over the range of low water saturation, as shown in Figure 4.3. However, the effect of permeability on the entry capillary pressure of steam is small (see Figure 4.3). Note that this analysis is based only on the results calculated using a scaling method instead of experimental data of steam-water capillary pressure measured directly in the geothermal rock samples. Hence the results need to be confirmed by direct measurement. However, the results shown in Figure 4.3 give us an understanding of the magnitude of the effect of the permeability on steam-water capillary pressure in geothermal rocks.

Figure 4.4 shows the comparison of the steam-water capillary pressure curve calculated using Equation 4.8 with that measured by Persoff and Hulen (1996) using an adsorption method at a temperature of 28.5°C. The porosity and permeability of the rock sample from The Geysers geothermal field that was used for the numbers in Figure 4.4 were 0.2% and 1.3 nd; the low range values measured by Persoff and Hulen (1996).
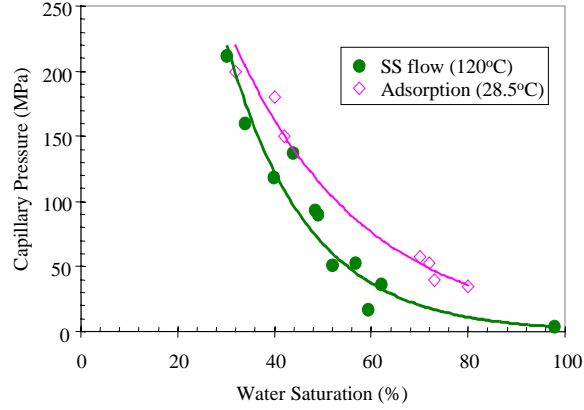
Figure 4.4: Steam-water capillary pressure curves by steady-state (SS) flow and adsorption methods for a rock sample from The Geysers field.

It is to be expected that the steam-water capillary pressure for a geothermal rock sample at the higher temperature of about 120°C is smaller than that at the lower temperature of 28.5°C, as shown in Figure 4.4. We scaled the experimental values of steam-water capillary pressure from Persoff and Hulen (1996) to the temperature of 120°C using Equation 4.9. The surface tension of steam/water at 120°C is 54.96 dynes/cm. The comparison of the steam-water capillary pressure for the Geysers rock by steady-state flow and adsorption methods is shown in Figure 4.5, based on the same temperature. The two sets of steam-water capillary pressure values are remarkably consistent after the temperature calibration.
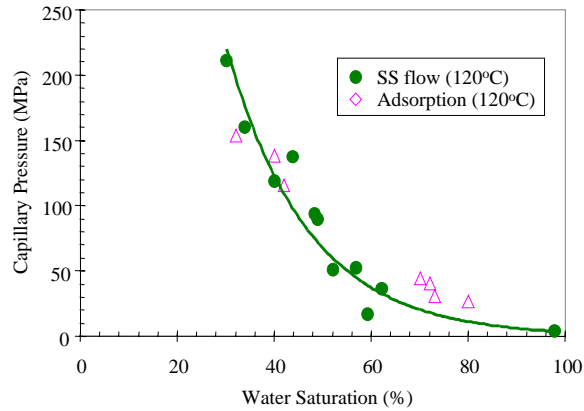
Figure 4.5: Comparison of steam-water capillary pressure curves by steady-state (SS) flow and adsorption methods for a rock from The Geysers field.

The consistency of the steam-water capillary pressure values shown in Figure 4.5 gives us confidence in applying these steam-water capillary pressure data in geothermal reservoir engineering, by the application of Equation 4.6. The purpose in using Equation 4.6 is that the reservoir rocks in geothermal fields have different porosity and permeability and it is impossible to measure the steam-water capillary pressure for every

rock sample. Therefore, we need to use Equation 4.6 to establish a correlation between the steam-water capillary pressure of rocks with different porosities and permeabilities.

It would be useful for geothermal reservoir engineers to have a technique to estimate the values of steam-water capillary pressure for geothermal rocks. This technique would be based on the experimental data and would be able to calculate steam-water capillary pressure for geothermal rocks with any porosity and permeability at any reservoir temperature. Until now, geothermal reservoir engineers have usually hypothesized the form of the steam-water capillary pressure curve used for numerical simulation, or ignored it entirely. In order to constitute such a steam-water capillary pressure model for geothermal rocks, we plotted all the steam-water capillary pressure data shown in Figure 4.5, including those measured by Persoff and Hulen (1996), vs. the normalized water saturation. The results are shown in Figure 4.6. The normalized water saturation is calculated using the following equation:

$$S_w^* = \frac{S_w - S_{wr}}{1 - S_{wr}} \tag{4.10}$$

where S_{wr} and S_w^* are the residual water saturation and normalized water saturation. The Brooks-Corey (1964) capillary pressure function is often used to model the capillary pressure curve; it is given by:

$$P_c = p_e (S_w^*)^{-1/\lambda} \tag{4.11}$$

where p_e is the entry capillary pressure and λ is the pore size distribution index. We used the Brooks-Corey capillary pressure function to fit the data. Figure 4.6 shows a match to all the data from this study and that of Persoff and Hulen (1996). The values of the best-fit parameters are $S_{wr} = 0.20$, $p_e = 13.96$ MPa and $\lambda = 0.669$. Note that these values are only valid when the normalized water saturation is expressed as a fraction rather than as a percentage.
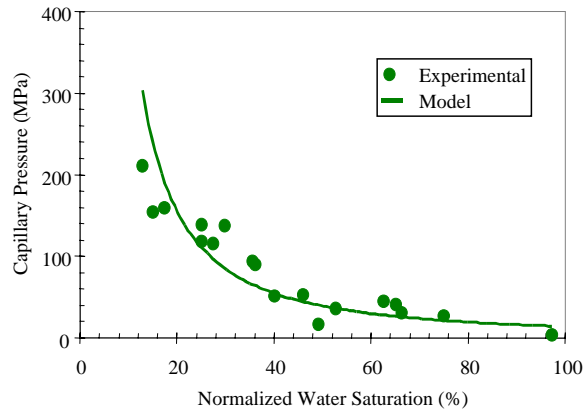

Figure 4.6: Normalized steam-water capillary pressure for a rock from The Geysers field.

40

Since the steam-water capillary pressure data shown in Figure 4.6 were obtained from a rock sample with a permeability of about 1.3 nd and a porosity of 0.2% at a temperature of 120°C, we would need to scale the data for rocks with different porosity and permeability or for different temperatures. This can be done using Equation 4.6. Using this approach, we have created a mathematical model of steam-water capillary pressure based on the experimental data from this study and from Persoff and Hulen (1996) for geothermal rocks as follows:

$$P_c = 6.475 \frac{\sigma}{\sqrt{\dfrac{k}{\phi}}} (S_w^*)^{-1.495} \tag{4.12}$$

where the units of P_c, σ and k are MPa, dynes/cm and nd respectively; ϕ and S_w^* are expressed as fractions. The porosity and permeability of reservoir rocks would need to be measured. The surface tension can be calculated once the reservoir temperature is known. Therefore, the steam-water capillary pressure curve for geothermal reservoir rocks may be obtained using Equation 4.12. It is assumed that the contact angle does not change with permeability and temperature.

4.6 DISCUSSION

The results of steam-water capillary pressure calculated by applying the Kelvin equation to the data from steady-state steam and water flow experiments are very preliminary, although Figure 4.5 shows remarkable consistency between the capillary pressure values obtained by steady-state flow and adsorption methods. The main uncertainties are the J-function and the contact angle in steam-water-Berea and steam-water-geothermal rock systems. If the difference of the J-function and the contact angle between the steam-water-Berea and steam-water-geothermal rock systems could be identified, then we could calculate the steam-water capillary pressure of geothermal rocks more accurately. It takes much less time and effort to measure the steam-water capillary pressure in highly permeable rocks than in low permeability rocks. Unfortunately, few data for the J-function and the contact angle in geothermal rocks are available. Hence, the application of the steam-water capillary pressure model (Equation 4.12) to geothermal reservoir engineering also depends on this further research on these parameters.

Another important question also remains: is there any difference between steam-water capillary pressure and air-water or nitrogen-water capillary pressure? If there is no difference, we could measure air-water capillary pressure as a substitute of the steam-water capillary pressure. The air-water measurements are very much easier to conduct. We have embarked on a project to measure the steam-water and air-water capillary pressures using the same rock sample.

4.7 CONCLUSIONS

Based on the present work, the following conclusions may be drawn:

1. It is possible to calculate steam-water capillary pressure by applying the Kelvin equation to the experimental data from the steady-state flow of steam and water in porous media.
2. The steam-water capillary pressure measured in the Berea sandstone sample with high permeability can be scaled to infer the steam-water capillary pressure in geothermal rocks with much lower porosity and permeability.
3. The steam-water capillary pressure scaled for a rock from The Geysers field using the data from steady-state flow experiments is consistent with that measured by Persoff and Hulen (1996) using an adsorption method. This implies that the *J*-functions of The Geysers rocks (matrix) may be similar to those of Berea sandstone.
4. A preliminary mathematical model has been developed for the steam-water capillary pressure in geothermal rocks based on the properties of a rock sample from The Geysers geothermal field.

4.8 FUTURE WORK

The next step is to set up an apparatus to be able to measure steam-water and air-water capillary pressure curves in the same core sample; the purpose is to identify the difference between steam-water and air-water capillary pressure.

5. SPONTANEOUS WATER IMBIBITION

This research project is being conducted by Research Associate Kewen Li and Professor Roland Horne. The objective of this project is to develop a method for calculating capillary pressure and relative permeability from spontaneous water imbibition data. In this report, we summarize the study regarding to spontaneous water imbibition.

5.1 SUMMARY

Spontaneous water imbibition into gas-saturated rocks is an important physical process during water injection into highly fractured geothermal and petroleum reservoirs. Few methods, however, are available for characterizing the process of spontaneous water imbibition into gas-saturated rocks. To this end, a method has been developed. Water relative permeability and capillary pressure can be calculated separately from water imbibition data using this method. A linear relationship between imbibition rate and the reciprocal of the gas recovery by spontaneous water imbibition was found and confirmed both theoretically and experimentally, even at different initial water saturations. The effect of initial water saturation on imbibition rate, residual gas saturation, and the gas recovery has been investigated. There was almost no effect of initial water saturation on residual gas saturation by spontaneous water imbibition. The higher the initial water saturation, the lower the water imbibition rate and the ultimate gas recovery. It was found that the capillary pressure did not vary with initial water saturation in a certain range. The capillary pressure calculated using the new method was approximately equal to the values measured using an X-ray CT technique in a glass-bead pack. The computed water relative permeability was consistent with published experimental results. The method developed in this study is also of importance for scaling-up experimental data.

5.2 INTRODUCTION

The reinjection of produced water into geothermal reservoirs, which are usually highly fractured, is a practical solution to the problems of reservoir pressure decline and environment impact. Spontaneous water imbibition phenomena exist in most of these reservoirs except those that are not water-wet; it is an important process driven by capillary forces. The study of spontaneous water imbibition is essential to predict the production performance in these reservoirs. Since the spontaneous imbibition is a capillary pressure dominated process, the imbibition rate is significantly dependent on the properties of the porous media, fluids, and their interactions. These include permeability and relative permeability of the porous media, pore structure, matrix sizes, shapes and boundary conditions, fluid viscosities, initial water saturation, the wettability of the rock-fluid systems, and the interfacial tension between the imbibed phase and the resident phase. Most of the studies in the literature focused mainly on oil-water-rock systems. Few methods are available for characterizing the process of spontaneous water imbibition into gas-saturated rocks. The method used usually is the Handy equation (Handy, 1960), that is, the weight or the volume of the imbibed water is proportional to the square root of the imbibition time:

$$N_{wt}^2 = A^2 \frac{P_c k_w \phi S_{wf}}{\mu_w} t \tag{5.1}$$

where A and N_{wt} are the cross-section area of the core and the volume of water imbibed into the core, respectively; ϕ is the porosity, μ_w is the viscosity of water and t is the imbibition time; k_w, P_c, S_{wf} are usually defined as the effective permeability of water, the capillary pressure, and the water saturation. These definitions of k_w, P_c, and S_{wf} may not be physically clear. For example, is S_{wf} the water saturation behind or in front of the water imbibition front? From the derivation of Eq. 5.15, it will be known that S_{wf} is the water saturation behind the imbibition front. k_w is the effective permeability of water phase at a water saturation of S_{wf}. Similarly, P_c is the capillary pressure at S_{wf}. Now, clear definitions are given to the parameters expressed in Eq. 5.1.

There are three main disadvantages to using the Handy equation to characterize spontaneous water imbibition. First, effective water permeability and capillary pressure can not be calculated separately from the spontaneous water imbibition test. Secondly, the straight line between the square of weight gain and the imbibition time often does not go through the origin, as it is supposed to. Thirdly, the relationship between the square of weight gain and the time is not a straight line during the later period of water imbibition, or even in the early period in some cases. Additionally, the amount of water imbibed into porous media is infinite when imbibition time approaches infinity, which is physically impossible.

Aronofsky et al. (1958) suggested an empirical form of the function of time relative to production from the matrix volume:

$$\eta = 1 - e^{-\lambda t} \tag{5.2}$$

where η is the recovery in terms of recoverable resident fluid by water imbibition, λ is a constant giving the rate of convergence, and t is the production time.

As pointed out by Kazemi and Gilman (1989), the equation proposed by Aronofsky et al. (1958) appeared to work well for history matching but did not generally reflect the physics of flow correctly. Using a numerical simulation technique, Chen et al. (1995) demonstrated that the Aronofsky et al. (1958) exponential relationship (Eq. 5.2) was only valid for cases with constant diffusion coefficients. Conducting water imbibition tests in the core samples from fissured oil fields, Iffly et al. (1972) showed that it was difficult to draw up the relationship between the recovery and dimensionless time using Eq. 5.2.

Schechter and Guo (1998) used a similar empirical equation to fit the experimental data of water imbibition in oil-saturated rocks:

$$\eta = 1 - e^{-\lambda t_D} \tag{5.3}$$

where t_D is the dimensionless time, defined as follows:

$$t_D = t \sqrt{\frac{k}{\phi}} \frac{\sigma \cos(\theta)}{\mu_m L_c^2} \qquad (5.4)$$

here k is the rock permeability, σ is the interfacial tension between oil and water, θ is the contact angle, μ_m is the geometric mean of water and oil viscosities and L_c is the characteristic length and defined as follows:

$$L_c = \sqrt{\frac{V}{\sqrt{\sum_{i=1}^{n} \frac{A_i}{X_{Ai}}}}} \qquad (5.5)$$

where V is the bulk volume of the matrix, A_i is the area open to imbibition at the ith direction, and X_{Ai} is the distance traveled by the imbibition front from the open surface to the no-flow boundary.

The scaling group in Eq. 5.4 was modified from Mattax and Kyte (1962), Ma et al. (1995), Gupta and Civan (1994). Ma et al. (1995) proposed the application of the geometric mean of the oil and water viscosities to the scaling group instead of only the water viscosity suggested by Mattax and Kyte (1962). Gupta and Civan (1995) included the contact angle in the scaling group of the dimensionless time. Eq. 5.4 was verified experimentally by Zhang et al. (1996) in oil-water-rock systems but not confirmed yet in gas-liquid-rock systems. Eq. 5.5 was modified from the shape factor suggested by Kazemi et al. (1989).

The main disadvantage of Aronofsky et al. (1958)-based functions is that the effective permeability or the relative permeability of water and capillary pressure may not be inferred from the experimental imbibition data.

In this study, a function has been derived to characterize the physical process of spontaneous water imbibition into air-saturated rocks. A linear relationship between the water imbibition rate and the reciprocal of the gas recovery by spontaneous water imbibition was found and confirmed both theoretically and experimentally, even at different initial water saturations. Based on this, a method has been developed to calculate separately the capillary pressure and the relative permeability of water phase at the water saturation behind the imbibition front from the spontaneous water imbibition data. The calculated capillary pressure and relative permeability were close to those measured experimentally. A lot of experiments of spontaneous water imbibition into air-saturated porous media (glass-bead pack and Berea sandstone) have been conducted at room temperature. The effect of initial water saturation on imbibition rate, residual gas saturation, and the gas recovery has been investigated.

5.3 THEORY

The function for characterizing the imbibition process of water into gas-saturated rocks is derived in this section. Assuming Darcy's law during the process of spontaneous water imbibition that occurs vertically upward in a core with a certain value of initial water

saturation, including the zero initial water saturation, the water imbibition velocity along the core sample is expressed as follows:

$$v_w = -\frac{k_w}{\mu_w}(\frac{\partial p_w}{\partial x} + \rho_w g)$$

(5.6)

where v_w is the flowing velocity of water phase; ρ_w is the water density; p_w is the pressure of water phase at the position x. From the definition of capillary pressure, the pressure of water phase can be calculated:

$$p_w = p_g - P_c$$

(5.7)

Substituting Eq. 5.7 into Eq. 5.6:

$$v_w = \frac{k_w}{\mu_w}(\frac{\partial P_c}{\partial x} - \frac{\partial p_g}{\partial x} - \rho_w g)$$

(5.8)

where p_g is the pressure of gas phase.

During the water imbibition, gas mobility is usually much greater than water mobility. If gas mobility is assumed to be infinite, the gas pressure gradient is estimated as:

$$\frac{\partial p_g}{\partial x} = -\rho_g g$$

(5.9)

where ρ_g is the gas density. Substituting Eq. 5.9 into Eq. 5.8:

$$v_w = \frac{k_w}{\mu_w}(\frac{\partial p_c}{\partial x} - \Delta\rho g)$$

(5.10)

where $\Delta\rho$ is the density difference between gas and water.

Schembre et al. (1998) and Akin and Kovscek (1999) used the X-ray CT method to monitor the process of water imbibition into air-saturated rocks that were assembled vertically upward; and reported that the CT images of diatomites and chalk showed a homogeneous and piston-like water front during the water imbibition. Our experimental results also showed that water imbibition would be a piston-like flow process. Based on these experimental observations, we may assume that water imbibes into air-saturated rocks in a piston-like manner at certain cases. In a piston-like imbibition flow, the following equation holds:

$$\frac{\partial P_c}{\partial x} = \frac{P_c}{x}$$

(5.11)

Substituting Eq. 5.11 into Eq. 5.10:

$$v_w = \frac{k_w}{\mu_w}(\frac{P_c}{x} - \Delta\rho g) \tag{5.12}$$

Assumed that the distribution of initial water saturation in the porous medium is homogeneous, the accumulated volume of water imbibed into the core with initial water saturation can be calculated as follows:

$$N_{wt} = Ax\phi(S_{wf} - S_{wi}) \tag{5.13}$$

where S_{wi} is the initial water saturation in the core. The water imbibition rate Q_w is equal to Av_w. Therefore, Eq. 5.13 can be expressed as:

$$Q_w = \frac{Ak_w}{\mu_w}(\frac{P_c}{x} - \Delta\rho g) \tag{5.14}$$

Substituting Eq. 5.13 into Eq. 5.14:

$$Q_w = \frac{dN_{wt}}{dt} = a\frac{1}{\eta} - b \tag{5.15}$$

where:

$$a = \frac{Ak_w(S_{wf} - S_{wi})}{\mu_w L}P_c \tag{5.16}$$

$$b = \frac{Ak_w}{\mu_w}\Delta\rho g \tag{5.17}$$

and

$$\eta = \frac{N_{wt}}{V_p} \tag{5.18}$$

where L and V_p are the core length and the pore volume of the core sample, respectively; η is the gas recovery by water imbibition in terms of pore volume. Eq. 5.15 may be appropriate for cocurrent spontaneous water imbibition into gas-saturated rocks with a piston-like imbibition front.

There is a linear relationship between the rate of the spontaneous water imbibition and the reciprocal of the gas recovery by water imbibition according to Eq. 5.15. This straight line is not forced to go through the origin; the value of the intersection point of this line on the axis of water imbibition rate should be negative. When the imbibition time approaches infinity, the reciprocal of the gas recovery approaches a finite value at which the water imbibition rate has a value that depends on the ratio of gravity and capillary

pressure gradients. Therefore, Eq. 5.15 avoids the infinite-value problem associated with Eq. 5.1.

From Eq. 5.15, we can see clearly the factors that affect water imbibition rate. These include the effective permeability (permeability and relative permeability), matrix size, capillary pressure (which is controlled by porosity, permeability, interfacial tension, and wettability), fluid viscosity, difference of density between gas and water (gravity), S_{wf} (which is influenced by permeability, pore structure, wettability, etc.), and initial water saturation.

Eq. 5.15 may be reduced to Eq. 5.1, the Handy function, when the gravity force is neglected. Our experimental results showed that gravity force can not be neglected in a lot of cases, depending on the ratio of gravity gradient and the capillary pressure gradient. Based on Eqs. 5.16 and 5.17, capillary pressure can be calculated:

$$P_c = \frac{1}{(S_{wf} - S_{wi})} \frac{a}{b} \Delta \rho g L \qquad (5.19)$$

The values of a and b in Eq. 5.19 can be calculated from the plot of imbibition rate and the reciprocal of the gas recovery. S_{wf} can be measured during the water imbibition test. Therefore, we can compute capillary pressure using Eq. 5.19.

According to Eq. 5.17, the effective water permeability at the water saturation of S_{wf} can be computed as follows:

$$k_w = \frac{\mu_w}{A \Delta \rho g} b \qquad (5.20)$$

A great challenge in characterizing imbibition behavior in gas-liquid systems was to calculate the effective water permeability k_w and capillary pressure P_c separately. The method (Eqs. 5.19 and 5.20) developed here provides a solution to this problem.

5.4 EXPERIMENTS

Fluids. Air was used as the gas phase and distilled water as the liquid phase in this study since the clay in the Berea sandstone core was deactivated by firing.

Core Samples. Two types of porous medium samples were used in this study. One was unconsolidated (glass-bead pack) and another was consolidated (Berea sandstone). The 90 mesh glass-bead pack had a gas permeability of about 25.7 darcy measured by nitrogen at a flow rate of 200 ml/min; its porosity was about 38.6 %; its length and diameter were 29.5 cm and 3.4 cm. The Berea sandstone sample had a permeability of around 1200 md and a porosity of about 24.5%; its length and diameter were 43.5 cm and 5.06 cm. The Berea sandstone sample was fired at a temperature of about 400°C to stabilize the clay in the core sample.

Apparatus. The structure of the glass-bead pack used in this study is shown in Fig. 5.1. It is known on the basis of the method that we developed in the last section that the effect of the sample cross-section area at the bottom on imbibition rate is significant (see Eqs. 5.15 and 5.16). In other words, the imbibition area of water should be equal to the cross-sectional area of the rock or the glass-bead sample. Experimentally, it has been found (Schembre et al., 1998) that there was a cone-shape distribution of water saturation at the bottom of a rock sample when water was introduced using a small tubing. This type of heterogeneous distribution of water would cause an error in calculating the effective water permeability and capillary pressure. Therefore, it is important to design the structure of the glass-bead pack to enable all the bottom part of the sample to be open to water. For this purpose, a lot of holes were drilled at the bottom of the glass cylinder, as shown in Fig. 5.1. In order to distribute the water more uniformly at the bottom of the glass-bead pack, a piece of filter paper was placed at the bottom.
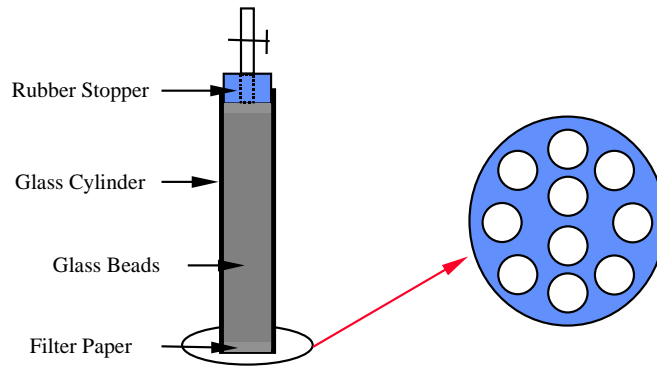
Figure 5.1: Schematic of the glass-bead pack

A schematic of the apparatus to conduct water imbibition tests in air-saturated porous media is shown in Fig. 5.2. The glass-bead pack sample was hung under a Mettler balance (Model PE 1600) which had an accuracy of 0.01g and a range from 0 to 1600 g. The water imbibed into the core sample was recorded in time by the balance using an under-weighing method and the real-time data were measured continuously by a computer through an RS-232 interface. The purpose of using the under-weighing method is to reduce the experimental error caused by water evaporation. Since the Berea sandstone sample used in this study was long and its weight was beyond the range of the Mettler balance, another balance (Sartorius, Model BP6100) with a larger capacity was used for the imbibition tests. This balance had an accuracy of 0.1g and a range from 0 to 6100 g.
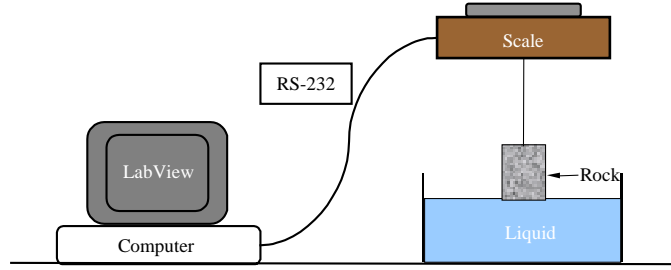
Figure 5.2: Schematic of apparatus for imbibition test.

The sample was not in contact with the water until the imbibition tests began. The water level in the container could be adjusted by raising or lowering the container using the adjustable jack under it. The data acquisition software used was LabView 4.1 by National Instrument Company.

The X-ray CT scanner used in this study for measuring the distribution of water saturation along the core was a Picker[TM] 1200 SX X-ray CT scanner with 1200 fixed detectors. The voxel dimension is 0.5 mm by 0.5 mm by 5 mm, the tube current used in this study was 50 mA, and the energy level of the radiation was 140 keV. The acquisition time of one image is about 3 seconds while the processing time is around 40 seconds.

The apparatus developed by Li and Horne (1999) for measuring steady-state gas-water relative permeabilities was used to establish certain initial water saturation in the Berea sandstone; a schematic is shown in Fig. 5.3. The value of water relative permeability calculated using Eq. 5.20 was compared with that measured by Li and Horne (1999) using a steady-state technique.
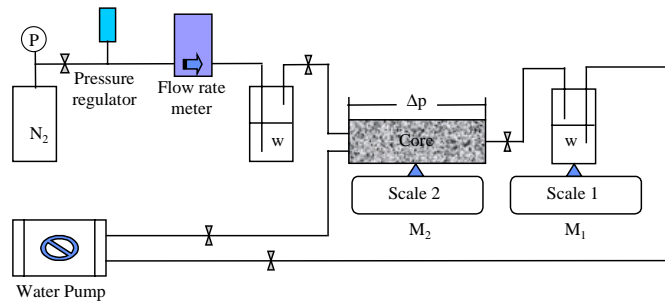

Figure 5.3: Schematic of the apparatus for establishing initial water saturation.

We could use the apparatus shown in Fig. 5.3 to establish a certain value of initial water saturation in the core samples either by single-phase gas flooding or two-phase gas-water simultaneous flooding. This will be discussed later in more details.

Procedure. The samples were dried by heating to a temperature of 105°C until their weight did not vary during eight hours or more. The glass-bead pack was assembled in the apparatus after it was cooled down, as shown in Fig. 5.2. The Berea sandstone sample was wrapped with heat-shrink tubing in order to avoid the water evaporation from the

side surface of the core sample. Two end plates were installed at the inlet and outlet of the core for fluid injection and production. Following that, the Berea sandstone was installed in the apparatus shown in Fig. 5.2. Water started to imbibe into the core once the bottom of the sample was brought in contact with the water surface by raising the water container. The weight change of the core sample was then recorded in time and used to calculate the effective permeability of water phase and the capillary pressure.

After the water imbibition test at zero initial water saturation for the Berea sandstone, the core was installed in the apparatus shown in Fig. 5.3 for the establishment of initial water saturation. The average water saturation in the core was monitored using the balance under the core system; the distribution of water saturation was then measured using the CT scanner from time to time. When the magnitude and the distribution of the water saturation in the core were satisfactory, the core was assembled in the apparatus shown in Fig. 5.2 to do the water imbibition test at this initial water saturation.

An X-ray CT scan was made at each centimeter along the sample that was positioned vertically before and after each water imbibition test. Finally, the sample was dried and another X-ray CT scan was made after completely resaturating with water. The CT values measured under three different states were used to calculate the porosity and the distribution of the water saturation as a function of height.

The procedure for the Berea sandstone was repeated at four different values of initial water saturation to study the effect of initial water saturation on the behavior of spontaneous water imbibition.

5.5 RESULTS

We conducted spontaneous water imbibition tests in both unconsolidated (glass-bead pack) and consolidated porous media (Berea sandstone) at room temperature. The experimental results and analysis are presented in this section.

Glass-Bead Pack. Fig. 5.4 plots the amount of water imbibition into the glass-bead pack as a function of time. Fig. 5.5 shows that the relationship between the water imbibition rate and the reciprocal of the gas recovery in the glass-bead pack is linear over a certain period of imbibition process, as prescribed by the theory developed in this study (Eq. 5.15). The linearity implies that the water imbibition front may be piston-like as it was assumed and as described previously by Schembre et al. (1998). We did observe the piston-like water imbibition front visually in the glass-bead pack during the early period of water imbibition. Another important feature shown in Fig. 5.5 is that the straight line does not go through the origin, as foreseen by Eq. 5.15. This feature demonstrates that the effect of the gravity force can not be neglected to characterize the process of spontaneous water imbibition in this glass-bead pack.
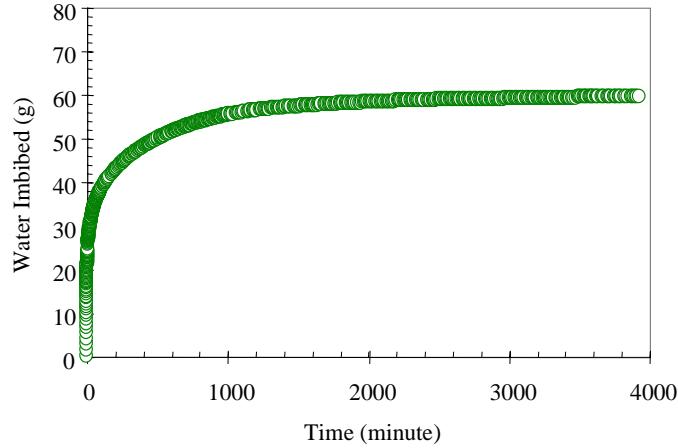
Figure 5.4: Water imbibition vs. time in a glass-bead pack.

At the initial stage of water imbibition, it is usually difficult to measure accurately the amount of water imbibed into the glass-bead pack or rock due to the influence of the buoyancy caused by inserting the sample into the water. There might be some error although the effect of buoyancy on the data was calibrated by weighing the sample after the water imbibition test. When the imbibition front reached a certain height in the glass-bead pack, the imbibition process might not be a capillary pressure-dominated process as we assumed in the mathematical derivation. The reason is that the effect of the gravity on the imbibition process increases with the increase of the height of the imbibition front. The water imbibition may be transferred from piston-like to diffusion-type. Eq. 5.15 is not appropriate to diffusion-type imbibition. This may explain why the relationship between the water imbibition rate and the reciprocal of production in a glass-bead pack shifts from the main trend at late time as shown in Fig. 5.5.
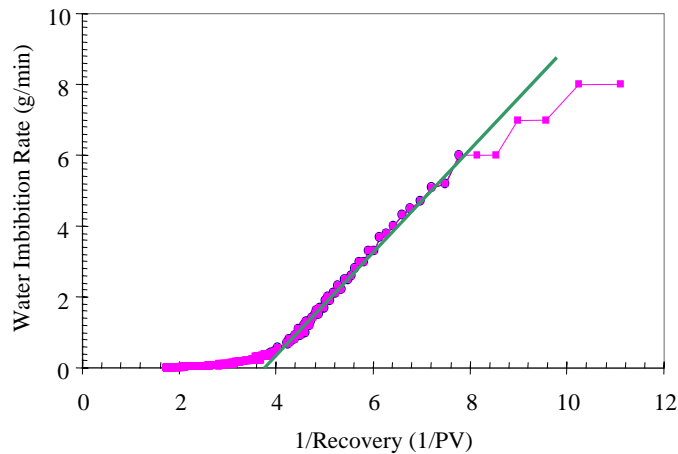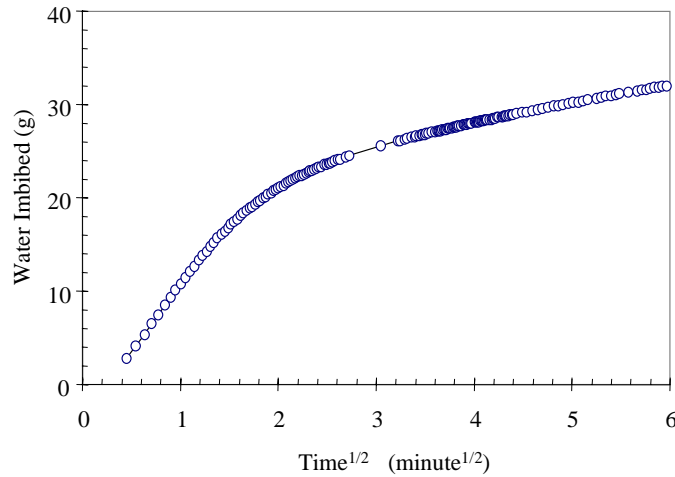

Figure 5.5: Water imbibition rate vs. the reciprocal of the gas recovery in a glass-bead pack.

The relationship between the water gain and the square root of imbibition time in the glass-bead pack is shown in Fig. 5.6. The time interval in Fig. 5.6 is about the same as

that corresponding to the linear section of the relationship in Fig. 5.5. There is no linear correlation between the amount of water imbibed and the square root of imbibition time for the same time interval, as suggested by the Handy function. There is a linear section during the first 2 or 3 minutes of imbibition (see Fig. 5.6), but the line does not go through the origin, as it is supposed to. This phenomenon may be brought about by gravity.

Figure 5.6: Water imbibition vs. the square root of time in a glass-bead pack.

According to Eq. 5.15, if a linear relationship does exist experimentally between water imbibition rate and the reciprocal of the gas recovery, the water saturation behind the imbibition front, S_{wf}, should be constant at different imbibition time. This implies that there is a section near the bottom of the sample but above the water contact level (see Fig. 5.2) where the water saturation does not change with the height. This can be confirmed by the saturation results measured by the X-ray CT scanner.

With the application of the method developed in this study (Eqs. 5.15 and 5.19), the imbibition capillary pressure at the water saturation behind the imbibition front calculated using the linear relationship shown in Fig. 5.5 is about 9.5 cm (water column). We will compare this value to the capillary pressure measured in the glass-bead pack using the X-ray CT technique.

Now we discuss the experimental results of the capillary pressure curve measured in the glass-bead pack. Hamon and Vidal (1986) reported that sample heterogeneity affected the water imbibition behavior in oil-water-rock systems. Therefore, the distribution of the porosity of the glass-bead pack from the bottom to the top was measured using the X-ray CT technique, which is shown in Fig. 5.7. The average porosity measured by the X-ray CT method was about 38.0%, which was consistent with the value of 38.6% measured by weighing the glass-bead pack before and after it was saturated with water. Fig. 5.7 shows that the glass-bead pack is homogeneous except a small part at the top. It will be demonstrated later that the water was not imbibed to this part.
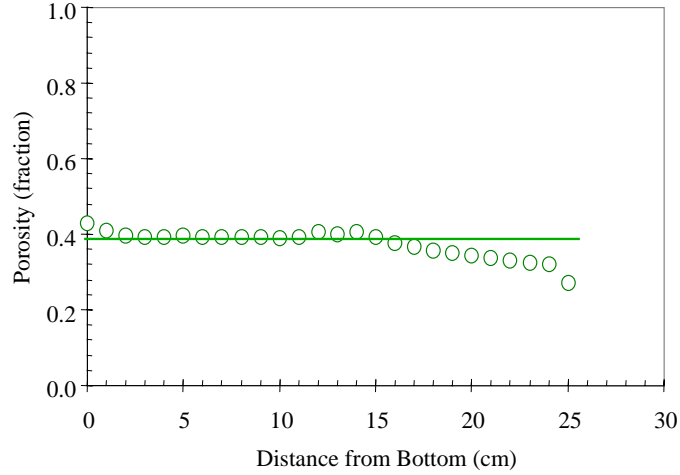
Figure 5.7: Porosity distribution in a glass-bead pack.

The distribution of CT values before and after the water imbibition test is shown in Fig. 5.8. CT_{dry} in this figure represents the CT value of the glass-bead pack when the sample is air-saturated and $CT_{objective}$ represents the CT value after the water imbibition was finished. The height in the pack at the point where the value of CT_{dry} is equal to the value of $CT_{objective}$ should stand for the capillary pressure at near zero water saturation (see Fig. 5.8). So the capillary pressure at near zero water saturation in the glass-bead pack is about 20 cm of water column.
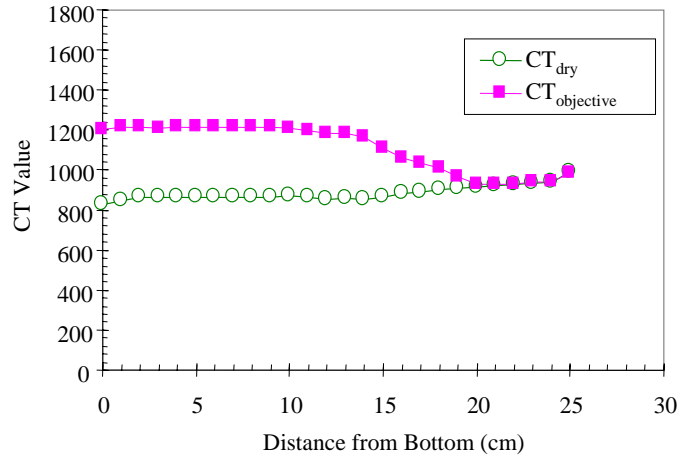

Figure 5.8: Distribution of CT values before and after imbibition test in a glass-bead pack.

It was assumed that the balance between the gravity force and the capillarity force was reached at any position along the glass-bead pack after the water imbibition was finished. Therefore, the capillary pressure at any position in the glass-bead pack was equal to the gravity force at the same position, which is the water column height at this point. The corresponding water saturation at this position was measured using the X-ray CT technique. The air-water imbibition capillary pressure curve of the glass-bead pack

54

measured using this method is plotted in Fig. 5.9. The air-water imbibition capillary pressure at zero water saturation is about 20 cm (water column). We can see from Fig. 5.9 that the air-water capillary pressure at the water saturation behind the imbibition front (actually the maximum water saturation), $P_c(S_{wf})$, is about 10 cm (water column). Therefore, the capillary pressure calculated using Eq. 5.15 is approximately equal to that measured using the X-ray CT method at the same water saturation of S_{wf}. This consistency proved the validity of the method developed in this study to calculate the capillary pressure using spontaneous water imbibition data.
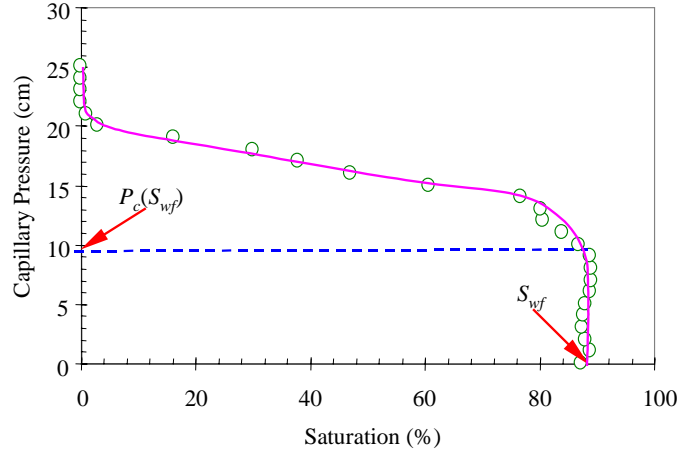

Figure 5.9: Air-water imbibition capillary pressure of a glass-bead pack.

The capillary pressure curve shown in Fig. 5.9 has some important features. First, all the water saturation points at the capillary pressure less than $P_c(S_{wf})$ have the same value. This is consistent with our prediction made previously, that is, there is a section near the bottom of the sample but above the water contact level where the water saturation does not change with the height. Secondly, the spontaneous water imbibition upward in a core with a length less than the water column height corresponding to $P_c(S_{wf})$ may be piston-like and a linear relationship exists between the imbibition rate and the reciprocal of the gas recovery. This mechanism might be also applied to actual reservoirs. If water is injected into a reservoir with a height less than the water column height corresponding to $P_c(S_{wf})$, there may be only one capillary pressure, $P_c(S_{wf})$, that governs the process of water injection into the matrix.

Using the features of the capillary pressure curve in Fig. 5.9, we may interpret why the water imbibition rate curve shown in Fig. 5.5 shifts from the main trend during the later period of water imbibition. When the capillary pressure is less than $P_c(S_{wf})$ during the early period, water saturation behind the imbibition front is constant (see Fig. 5.9). Therefore, the effective permeability of water and the capillary pressure do not change with the imbibition time. According to Eqs. 5.15, 5.16, and 5.17, the slope and the intersection of the water imbibition rate curve are kept constant. When the capillary pressure is greater than $P_c(S_{wf})$ at later time, water saturation behind the imbibition front decreases sharply along the sample with imbibition time. Therefore, the effective permeability of water phase decreases with the imbibition time. The capillary pressure

does not increase much with the decrease of the water saturation (see Fig. 5.9). As a result, the water imbibition rate decreases with time at a different rate or gradient from that at the early period, which is shown in Fig. 5.10. According to Eqs. 5.15, 5.16, and 5.17, the slope and the intersection of the water imbibition rate curve also vary with time or the reciprocal of the gas recovery, $1/\eta$, in the later period of water imbibition (see Fig. 5.5). Fig. 5.10 shows that the water imbibition rate decreases much faster at early time than at later time in the glass-bead pack.
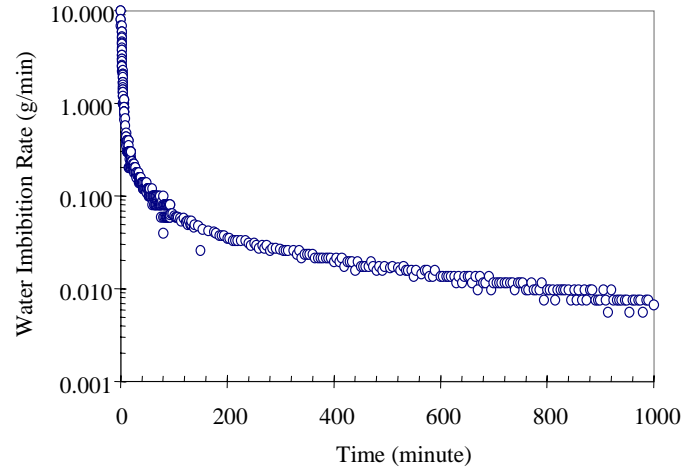

Figure 5.10: Water imbibition rate vs. time in a glass-bead pack.

Berea Sandstone. Water imbibition tests at different initial water saturations were conducted in a fired Berea sandstone sample. The experimental results are discussed in this section.

The X-ray CT method was used to measure the distribution of porosity and the water saturation in the core. Fig. 5.11 shows the porosity distribution in the core. It can be seen that this core was homogeneous enough to be used to conduct water imbibition tests.
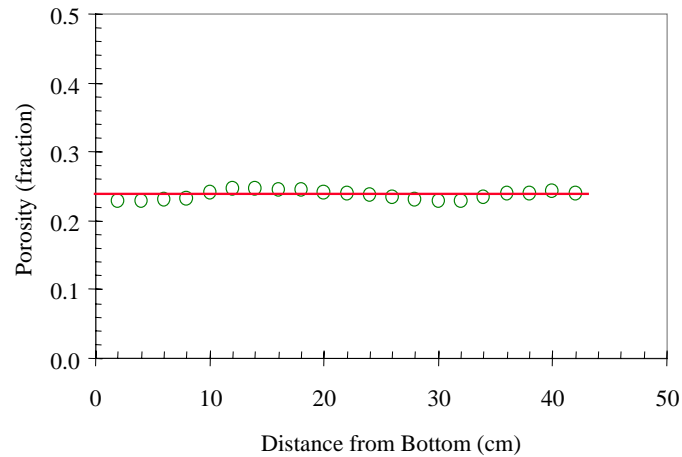

Figure 5.11: Porosity distribution in Berea.

56

We first tried to establish initial water saturation in the core by injecting only air. The direction of air flow was varied by injecting alternately from each end of the core. This technique for establishing initial water saturation worked well in a 10 cm long sandstone core based on our experience. However, it was not clear whether it was suitable for a 43.5 cm long core sample. The distribution of water saturation (S_w) in the core is shown in Fig. 5.12, which shows that the water saturation was not homogeneous at either of the two water saturation values. The values of S_w shown in Fig. 5.12 are the average water saturations in the core measured by the X-ray CT method, which are consistent with the average water saturations measured using the weight change of the core before and after complete saturation by distilled water. Fig. 5.12 shows that it is almost impossible to establish a homogeneous distribution of initial water saturation in a long core by single-phase air injection. Therefore, we started to use a steady-state technique, that is, air and water were injected simultaneously into the core with a specific ratio of air to water flow rates using the apparatus shown in Fig. 5.3. One of the established initial water saturation points is shown in Fig. 5.12 (solid squares). Compared with the distributions of initial water saturation established by single-phase (1-P) air injection, it can be seen that the two-phase (2-P) air-water simultaneous injection technique could establish a more homogeneous distribution of water saturation than single-phase air injection in the core.
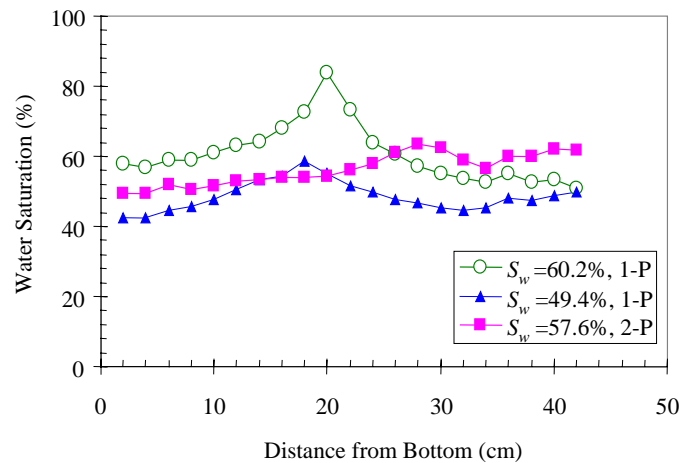

Figure 5.12: Distribution of S_w *in Berea using single-phase air and two-phase air-water simultaneous injection methods.*

Water imbibition tests were conducted after the initial water saturation in the core was established. The relationship of water gain vs. imbibition time is shown in Fig. 5.13 for different values of initial water saturation. The absence of initial water saturation between 0 and 38.6% was due to the difficulty in establishing the low initial water saturation with a homogeneous distribution in such a long core using either single-phase air or two-phase air-water injection method.
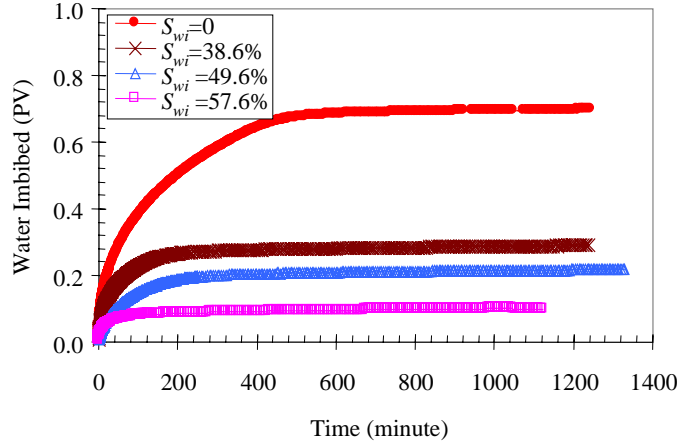
Figure 5.13: Water gain vs. time in Berea at different initial water saturations.

It can be seen from Fig. 5.13 that the amount of water imbibed into the core sample and the time that water gain reached the maximum value decreased with an increase of initial water saturation.

The water imbibition rate vs. the reciprocal of the gas recovery is shown in Fig. 5.14. This figure demonstrates that the relationship between the imbibition rate and the reciprocal of the gas recovery in a Berea sample is linear at different initial water saturations, as expected from the model developed in Eq. 5.15.
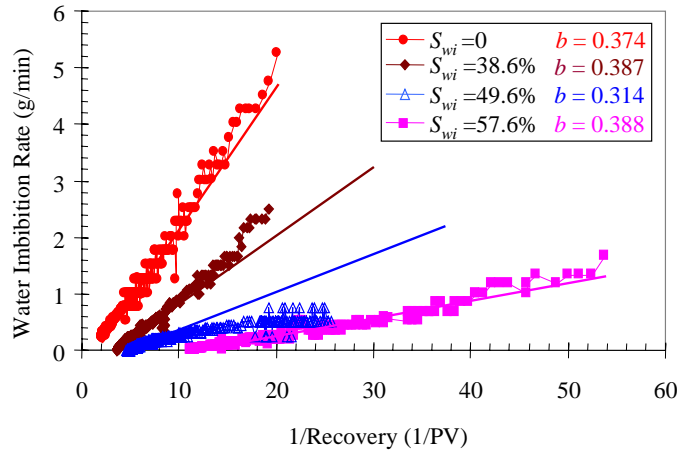
Figure 5.14: Water imbibition rate vs. the reciprocal of the gas recovery at different initial water saturations in Berea.

Linear regression was made for the relationship between the water imbibition rate and the reciprocal of the gas recovery at each initial water saturation point. The values of b are presented in Fig. 5.14. The non-zero values of b show that the straight lines do not go through the origin. This implies that the effect of gravity can not be neglected in this core with a permeability of about 1200 md. Our recent experimental results have shown that the effect of gravity might not be neglected even in a core with a permeability of about

58

500 md. This might be interpreted using Eq. 5.15. The effect of gravity on imbibition rate may be neglected when the gravity gradient is small enough compared to the capillarity gradient at S_{wf} according to Eq. 5.15. When the permeability of the core is low, S_{wf} may be high and then $P_c(S_{wf})$ may be low in the core. Therefore, the effect of gravity on water imbibition rate may not be neglected even in a core with low permeability. However, the effect of gravity on water imbibition rate may decrease with the permeability, which depends on other factors such as wettability.

Also shown in Fig. 5.14 is the effect of initial water saturation on the water imbibition rate. The higher the initial water saturation, the lower the imbibition rate. Note that the unit of the water imbibition rate here is g/min instead of GOIP/min. Schembre et al. (1998) observed a similar phenomenon and stated that the imbibition in diatomite was relatively rapid when initial water saturation was low due to large capillary pressure. We will show later that the capillary pressure governing water imbibition does not change with initial water saturation in a certain range.

An interesting phenomenon observed in Fig. 5.14 is that the value (b) of the intersection of the straight line changed very little with initial water saturation. Actually, the value of b should be constant because it depends only on the effective water permeability (see Eq. 5.15) while the effective water permeability only depends on the water saturation behind the imbibition front that may not change with initial water saturation. The rock permeability is easy to measure; so the water relative permeability at this water saturation could also be calculated from the water imbibition test. The average effective water permeability calculated using the values of b shown in Fig. 5.14 was about 316.8 md and the imbibition relative permeability of water was about 0.264; the corresponding residual gas saturation by spontaneous water imbibition was about 33.5%. These values are remarkably consistent with those measured by Li and Horne (1999), Horne et al. (2000) using nitrogen-water in a Berea sandstone sample with almost the same permeability using a steady-state method. The residual gas saturation and the corresponding water relative permeability that Li and Horne (1999) measured at the same temperature during the water imbibition circle were about 30% and 0.261, respectively. This consistency confirmed the validity of Eq. 5.15 and the method to compute the relative permeability of water phase at residual gas saturation from spontaneous water imbibition data.

At the initial water saturation of 49.6%, however, the relationship between the imbibition rate and the reciprocal of the gas recovery shown in Fig. 5.14 is not linear at earlier time. The reason for this phenomenon may be due to the heterogeneous distribution of initial water saturation in the core. The distribution of water saturation in the core before and after the water imbibition tests measured using the X-ray CT technique is plotted in Fig. 5.15.
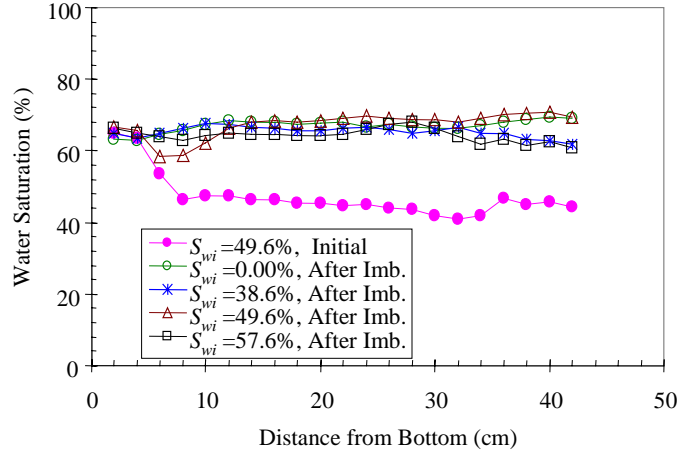
Figure 5.15: Distribution of water saturation before and after imbibition in Berea at different initial water saturations.

For comparison, the distribution of water saturation in the core after water imbibition at different initial water saturations is also shown in this figure. The distribution of initial water saturation with a value of 49.6% was not homogeneous in the region near the bottom where the water imbibition started. It took more than 40 hours to establish the initial water saturation by simultaneous injection of air and water from the top of the core. The heterogeneous distribution of initial water saturation shown in Fig. 5.15 may be due to the capillary end effect in multiphase flow. The water saturation near the bottom region was about 63.6%, very close to the maximum water saturation (about 66.5%) that the imbibition could reach in this type of rock. This region with high water saturation might behave as a barrier for water imbibition, which could reduce the imbibition rate at the beginning of the imbibition process according to Eq. 5.15.

In order to avoid the barrier (formed by a high water saturation region) for water imbibition, air and water were injected simultaneously from the bottom of the core to establish the other initial water saturation. This idea was based on the observation in Fig. 5.15 that the distribution of water saturation at the position about 3 cm away from the outlet was very homogeneous. It can also be seen from Fig. 5.15 that the distributions of water saturation after imbibition at different initial water saturations from 0 to 57.6% were almost the same.

Note that only the points in the later period of water imbibition at the initial water saturation of 49.6% were used to do the linear regression to calculate the values of the slope and the intersection (see Fig. 5.14). These values were used to calculate the corresponding capillary pressures using Eq. 5.15. The calculated capillary pressure vs. initial water saturation is plotted in Fig. 5.16. Although there are only four points in Fig. 5.16, we can see that the capillary pressure was not influenced significantly by the initial water saturation over a wide range from 0 to 57.6%. This may be explained as follows. It is the capillary pressure at the water saturation behind the imbibition front that controls the process of water imbibition instead of the capillary pressure at the water saturation in front of the imbibition front. The experimental results demonstrate that the water

60

saturation behind the imbibition front was almost unaffected by the initial water saturation (see Fig. 5.15). Otherwise, the relationship between the water imbibition rate and the reciprocal of recovery shown in Fig. 5.14 would not be linear. For a given core, capillary pressure only depends on the water saturation. Therefore, the capillary pressure calculated using Eq. 5.15 does not change with the initial water saturation in the core.
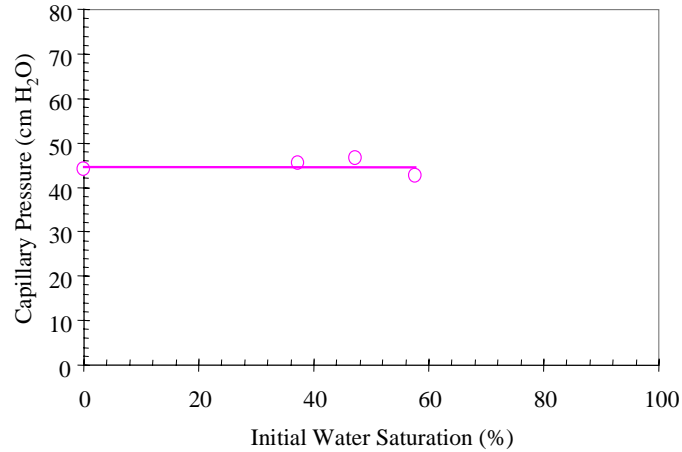

Figure 5.16: Effect of initial water saturation on the capillary pressure in Berea.

The values of the maximum water saturation (S_{wmax}) that could be reached by the spontaneous water imbibition at different initial water saturations are shown in Fig. 5.17. The maximum water saturation in the core by spontaneous water imbibition does not vary with initial water saturation; it depends on rock permeability, pore structure, interfacial tension between the two fluids, and wettability. Therefore, maximum water saturation by spontaneous water imbibition may be one of the important parameters to estimate the ability to inject water into reservoirs.
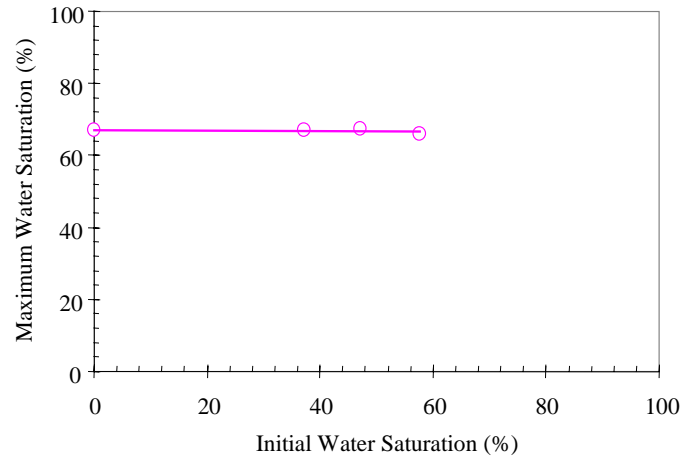

Figure 5.17: Effect of initial water saturation on the maximum water saturation in Berea.

The gas recovery by spontaneous water imbibition is expressed as follows:

$$\eta_\infty = \frac{S_{w\max} - S_{wi}}{1 - S_{wi}} \tag{5.21}$$

where η_∞ is the ultimate recovery by spontaneous water imbibition. Since the maximum water saturation is not affected by the initial water saturation, the gas recovery decreases with the increase of initial water saturation based on Eq. 5.21, which is shown in Fig. 5.18. Li and Firoozabadi (2000) also observed this phenomenon for both oil and water imbibition in air-saturated rocks.
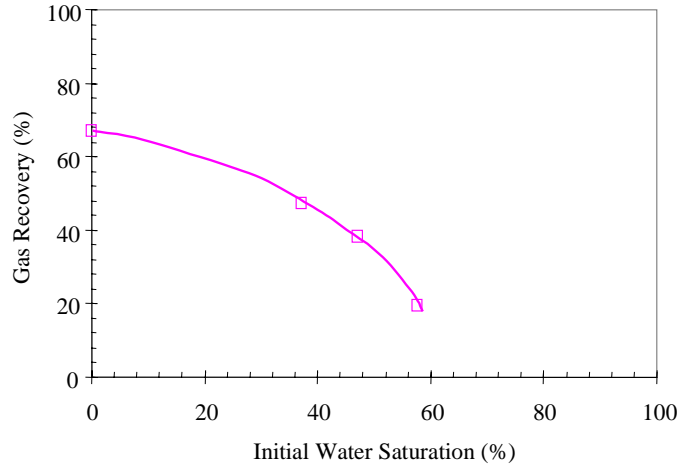

Figure 5.18: Effect of initial water saturation on the gas recovery in Berea.

5.6 DISCUSSION

Only one point of capillary pressure and relative permeability governs the spontaneous water imbibition into water-wet porous media according to the experimental results in this study. This may be important to the reservoir engineering of water injection because the spontaneous water imbibition is a major physical process during water injection into highly fractured geothermal reservoirs. Knowing that spontaneous water imbibition depends on only one capillary pressure and relative permeability, we may just need to know one capillary pressure and relative permeability value for the matrix to do the corresponding reservoir engineering calculation. These two values could be obtained from water imbibition data.

There may be other significance to the fact that only one point of capillary pressure and water relative permeability govern the water imbibition behavior at different initial water saturations. Since only one point of capillary pressure and water relative permeability govern the water imbibition behavior, it may not be reasonable to infer the whole capillary pressure and relative permeability curves from the water imbibition tests in air-saturated rocks by using the technique of automatic history matching. This type of method has been often used in reservoir engineering. One common phenomenon in the application of automatic history matching to infer capillary pressure and relative permeability curves is multiple solutions. That only one point of capillary pressure and water relative permeability governs the water imbibition behavior may be one of the reasons for the multiple solution problem.

5.7 CONCLUSIONS

Based on the present work, the following conclusions may be drawn:

1. The relationship between the water imbibition rate and the reciprocal of the gas recovery is linear at different initial water saturations from 0 to 57.6% in Berea. This relationship might be used to characterize the spontaneous water imbibition into gas-saturated porous media.

2. A method has been developed to calculate separately the capillary pressure and the relative permeability of water phase at S_{wf} from the imbibition data. The method has been confirmed experimentally in Berea and a glass-bead pack. The calculated capillary pressure and the relative permeability were nearly equal to those measured.

3. The effect of gravity on water imbibition behavior may not be neglected in gas-water-rock systems, even if the rock permeability is not very high.

4. The maximum water saturation by the spontaneous imbibition is almost unaffected by initial water saturation in Berea; the ultimate gas recovery decreases with the increase of initial water saturation.

5. The capillary pressure and the relative permeability governing the spontaneous water imbibition in Berea may not vary with S_{wi}. Therefore, the water imbibition may be governed by only one point of capillary pressure and relative permeability. This may be of significant application to reservoir engineering.

6. It may be difficult, in certain cases, to infer unique curves of capillary pressure and relative permeability from imbibition data because there may be only one point of capillary pressure and relative permeability governing the spontaneous imbibition.

5.8 FUTURE WORK

We are developing the apparatus for conducting spontaneous water imbibition in steam-water systems instead of air-water systems.

6. RELATIVE PERMEABILITY IN SMOOTH-WALLED FRACTURES

This project is being conducted by Research Assistant Gracel P. Diomampo, Research Associate Kewen Li and Prof. Roland Horne. The goal is to gain better understanding of steam-water flow through fractured media and determine the behavior of relative permeability in fractures.

6.1 BACKGROUND

Geothermal reservoirs are complex systems of porous and fractured rocks. Complete understanding of geothermal fluid flow requires knowledge of flow in both types of rocks. Many studies have been done to investigate steam and water flow through porous rocks. This is not the case for multiphase flow in fractures. Only a few published data are available most of which have been done for air-water system or for water-oil systems. Earliest is Romm's (1966) experiment with kerosene and water through an artificial parallel-plate fracture lined with strips of polyethylene or waxed paper. Romm found a linear relationship between permeability and saturation, $S_w = k_{rw}$, $S_{nw} = k_{rnw}$ such that $k_{rw} + k_{rnw} = 1$. Pan et al. (1996) performed a similar experiment with an oil-water system but arrived at conflicting results. Significant phase interference was observed such that $k_{rw} + k_{rnw} < 1$. Both studies, however, conclude that residual saturations are zero such that a discontinuous phase can flow as discrete units along with the other phase.

In an attempt to develop a relationship between fracture relative permeability and void space geometry, Pruess and Tsang (1990) conducted numerical simulation for flow through rough-walled fractures. Their study shows the sum of the relative permeabilities is less than 1, residual saturation of the nonwetting phase is large and phase interference is greatly dependent on the presence or absence of spatial correlation of aperture in the direction of flow. Persoff et al. (1991) did experiments on gas and water flow through rough-walled fractures using transparent casts of natural fractured rocks. The experiment showed strong phase interference similar to the flow in porous media. Data of Persoff (1991) and Persoff and Pruess (1995) for flow through rough-walled fractures were compared in Horne et al. (2000), as shown in Figure 6.1.

Presently, the mechanism of flow and the characteristic behavior of relative permeability in fractures are still undetermined. Issues such as whether a discontinuous phase can travel as discrete units carried along by another phase or will be trapped as residual saturation as in porous medium are unresolved. The question of phase interference i.e. is the relative permeability curve against saturation an X-curve, Corey or some other function is still unanswered. The main objective of this study is to contribute to the resolution of these issues. Experiments on flow through smooth-walled fractures will be done first for air-water flow with the aim of establishing a reliable methodology for flow characterization and permeability calculation. Then these experiments will be done with a steam-water system; and with rough-walled fractures.
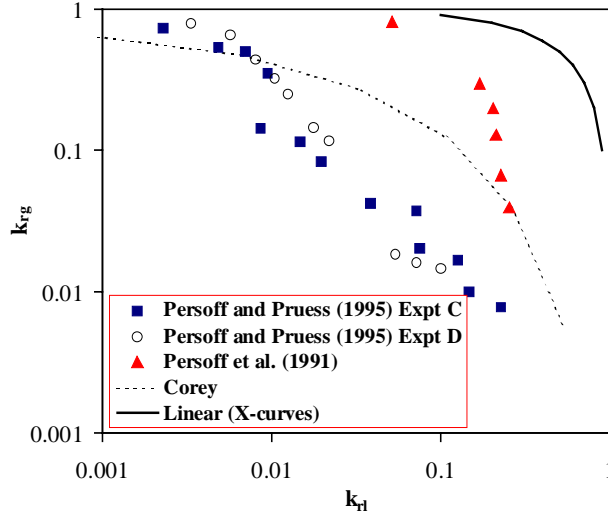
Figure 6.1: Some measurements of air-water relative permeabilities in rough-walled fractures (graph from Horne et al., 2000).

6.2 EXPERIMENTAL APPARATUS AND MEASUREMENT TECHNIQUES

The apparatus consists of a 183 cm by 31 cm of horizontal glass plate on top of an aluminum plate. The aperture is dictated by 0.2-mm thick shims inserted in between the glass and aluminum plates. The shims were placed along the boundaries and in three columns along the flow area. It should be noted that the shims placed as columns along the plate do not divide the plate into separate flow sections. This was deduced upon observing cross flow along the shims.

The sides of the plates are sealed together with a silicone adhesive. It was observed that even with the adhesive, the inlet head has to be kept below 15 cm to avoid leakage. This presents a maximum limit in the flow rates approximately 2 cc/sec for water and 9 cc/sec for nitrogen.

Horizontal slits in the ends of the metal plate serve as entry and exit points for the fluids. There are two available canals for input of gas and liquid. The options to input nitrogen and water as separate streams or as mixed fluid in a single stream were tried. It was found that mixing the gas and water prior to input caused no significant improvement in fluid distribution. Thus, the gas and water streams were injected separately for simplicity, ease of flow rate control and inlet pressure reading.

Gas flow was controlled through a flow regulator. The liquid rate was regulated by maintaining a constant head in the water reservoir and by use of a needle valve. Dye was injected in the water stream for better phase identification. Figure 6.2 is a schematic diagram of this configuration.
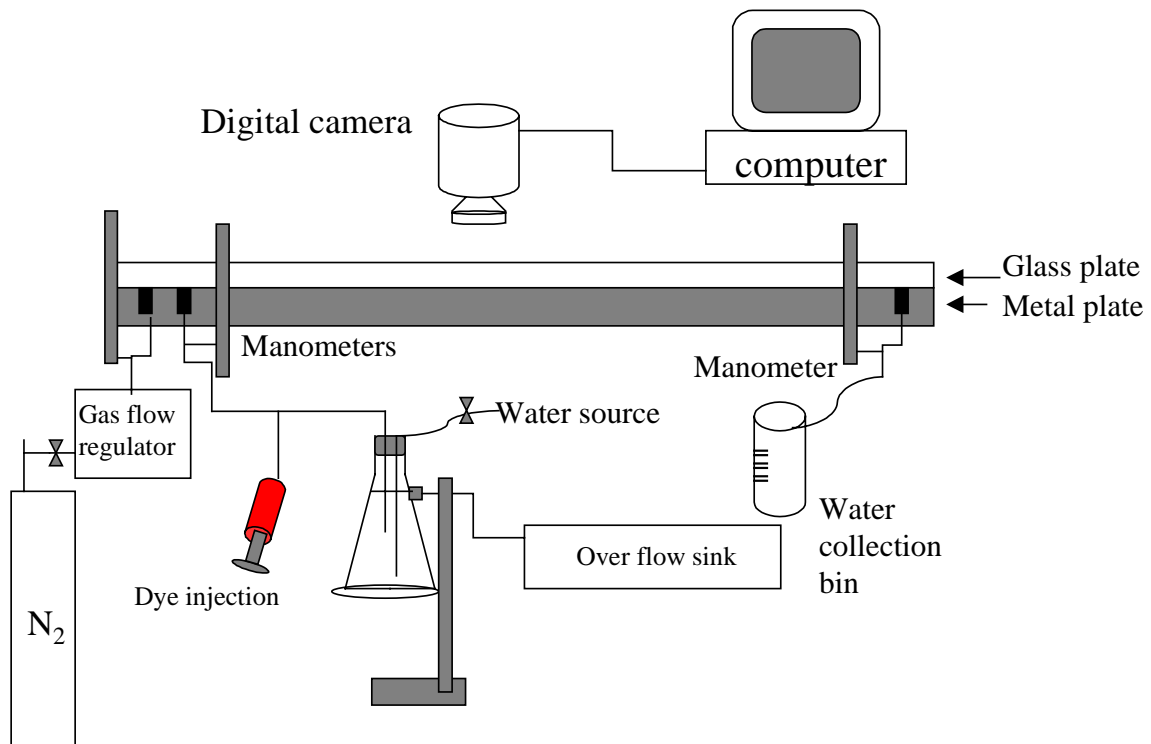
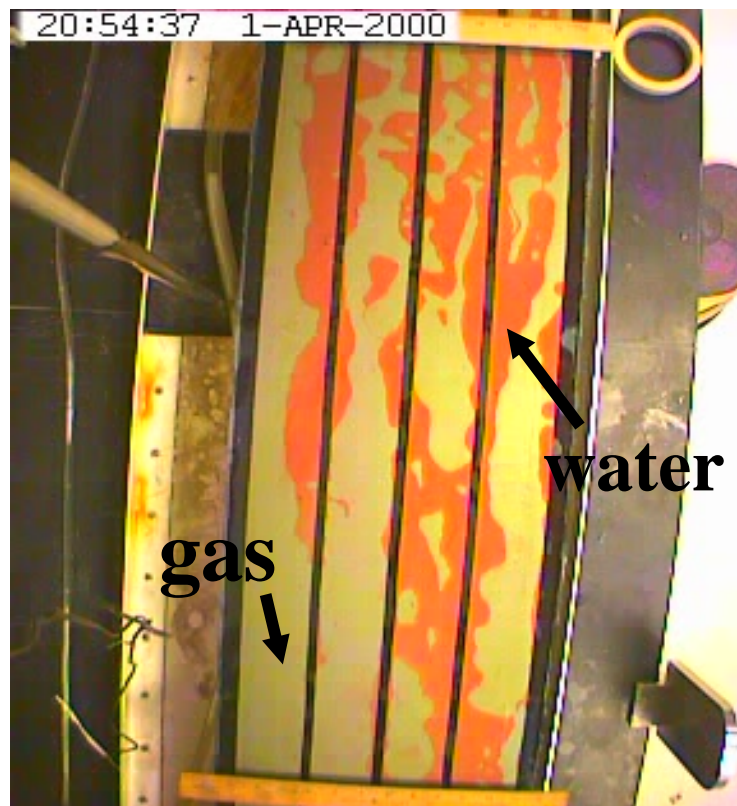*Figure 6.2: Apparatus for air and water flow through smooth walled fractures.*

Figure 6.3: Sample camera image for two-phase run.

Pressures were read through manometers located at each end of the metal plate through tees in the outlet and inlet tubing. Water flow rate was measured by collection and weighing of the outgoing stream. Gas flow rate was read directly in the flow regulator.

Saturation was computed by measuring the area that each phase occupied. This was done by taking digital photographs of a constant area of the plate at a particular gas and water rate. The area is around 3 ft. long. It was chosen far enough from the ends of the plates to prevent end effects. Figure 6.3 shows a sample photo of a two-phase run. The photographs were processed in a Matlab program. The program uses quadratic discriminant analysis to group the pixels of the photograph into three groups: the water phase, gas phase and the shim. The grouping was based on color differences. Saturation was calculated as total pixels of liquid group over the sum of the gas and liquid group. Figure 6.4 is a comparison of the gray scaled image produce by the program and the original photograph from the digital camera. The accuracy of the program in calculating the saturation can be related to the similarity in details of the gray scale image to the true image. From the figure, it can be said that the program has reasonable accuracy.
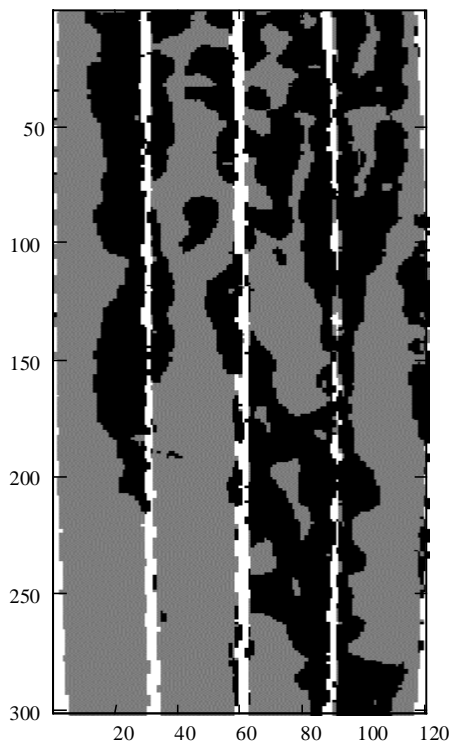
Saturation = 0.5987
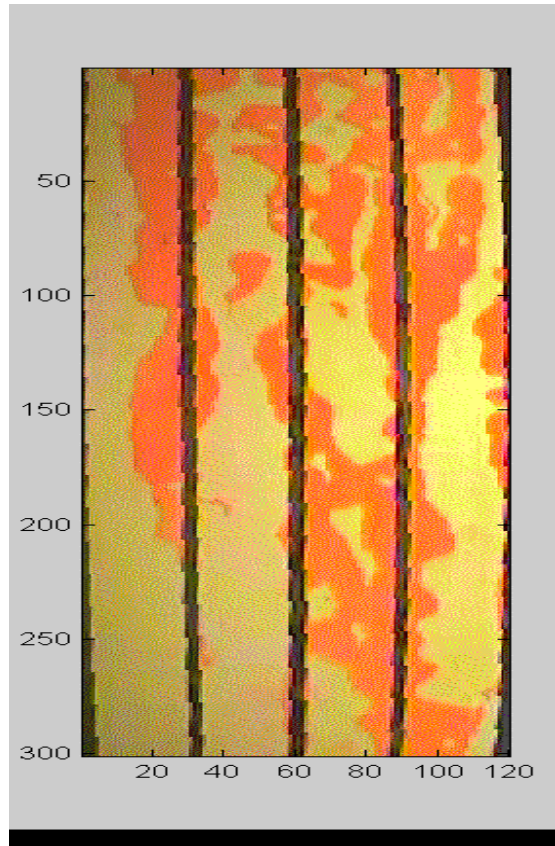
Figure 6.4: Comparison of gray image produced by Matlab program to actual photo taken by digital camera.

Pan et al. (1996) also used this technique for measurement of saturation. This study noted that the sources of error in this technique were the quality of the photographs and the water film adsorbed on the surfaces of the plates with the latter being of minimal

effect. Good quality photographs are the ones with clear distinction between the gas and liquid phases. The use of dyed liquid enhanced visualization of phase boundaries and produced quality photographs.

6.3 PARTIAL RESULTS AND DISCUSSION

Preliminary experiments were done with q_{gas}/q_{liq} values of 1, 5, 10, 20 and single-phase runs at residual saturation. There were some important observations:

In these ratios of q_{gas}/q_{liq}, the water and gas phase travel along the plate as separate channels. These separate flow paths change with time and position. This is illustrated in the series of images in Figure 6.5, which were taken at constant gas and liquid rate. This observation imply that at these ratio, phases move individually and not as "moving islands" or "globules" of the discontinuous phase carried along by the other phase. It also suggests that there is no local steady-state saturation.
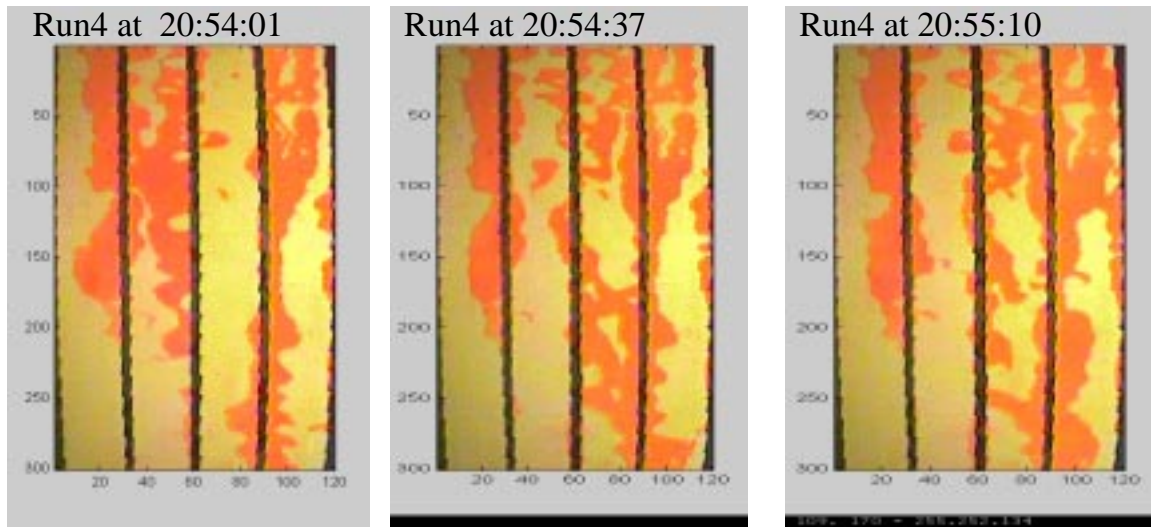
Figure 6.5: Images at constant gas and liquid rate in short time intervals to illustrate changes in the gas and liquid flow paths.

These fast changes in flow paths are accompanied by pressure fluctuations. When the gas has established enough energy to break through the water flow path, there is a corresponding increase in inlet gas pressure and decrease in water line pressure. The same is true when the water phase breaches through gas channels. This has caused difficulty in obtaining pressure data from the manometers, and represents a likely source of error in pressure data.

Residual saturations obtained were very low. S_{wr} is around 0.02-0.06. Similarly, S_{gr} is around 0.04-0.06. This indicates that there is negligible trapping in this smooth-walled fractures.

Pan et al. (1996) discussed two approaches in data analysis: the porous medium approach where Darcy's law is used and the homogeneous single-phase approach where the system is treated as a single-phase pipe flow. Because of the observations in the experiments, it seemed appropriate to treat the data using porous medium approach.

Darcy's law was used to obtained the single-phase and two-phase liquid permeability:

$$k_l = \frac{q_i \mu L}{(p_i - p_o)} \tag{6.1}$$

subscripts 'o' stands for outlet and 'i' for inlet, μ the viscosity, p as pressure, L for length of the plate and q as Darcy flow velocity from

$$q_o = \frac{Q_o}{bw} \tag{6.2}$$

where Q is the volumetric rate, b the aperture and w as the width of the plate.

The relative permeability is then calculated by taking the ratio of the two-phase k_l with the single-phase k_l.

The gas permeability was calculated using the equation from Scheidegger (Scheidegger, 1974):

$$k_g = 2q_o \mu L \frac{p_o}{p_i^2 - p_o^2} \tag{6.3}$$

Similarly, taking the ratio of the two-phase k_g with single-phase run gives the relative permeability.

The complete list of calculated relative permeability values, their corresponding saturation range is shown in Table 6.1. Figures 6.6 and 6.7 shows the plot of these data along with the X-curves. The data is clustered at small saturation range and lies far from the X-curves.

6.4 FUTURE WORK

Further experiments with nitrogen-water system will be done at higher order of variation of q_{gas}/q_{liq}. This is to obtain wider saturation range in the relative permeability values. This requires additional control in the water rate. This will be achieved by replacing the constant head reservoir with a meter pump that can consistently deliver smaller water rates. Also, to facilitate pressure reading at low water saturation, a low range pressure transducer will be used instead of a manometer for the water inlet line. After the nitrogen-water experiments, the apparatus will be further modified for steam-water system.
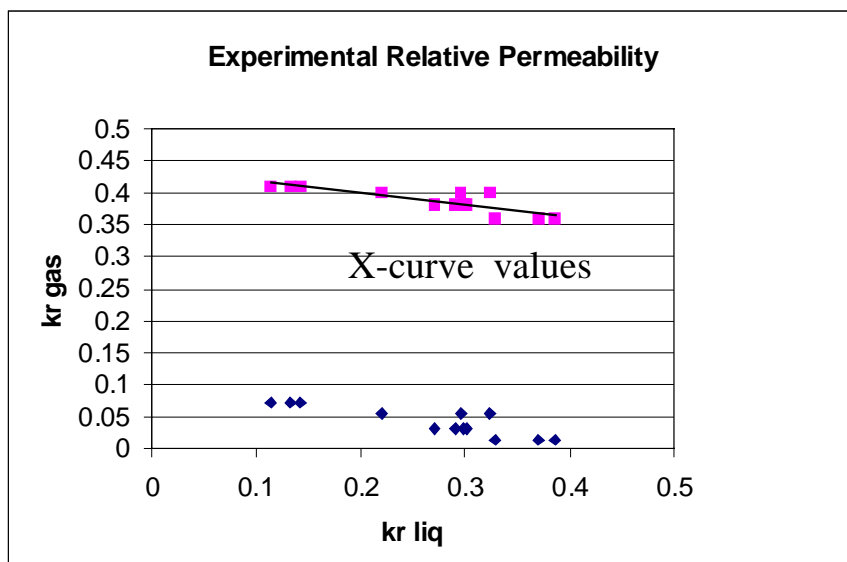
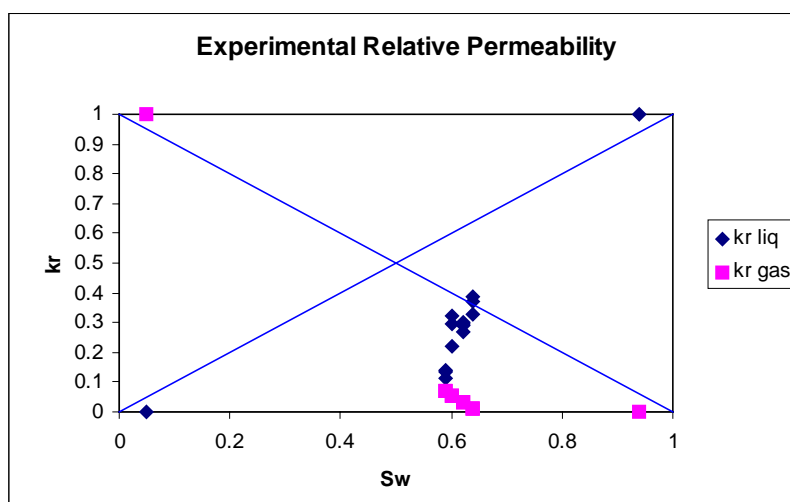*Figure 6.6: Comparison of experimental relative permeability values with X-curve values.*

Figure 6.7: Experimental relative permeability values against saturation.

Table 6.1 Calculated relative permeability values.

run #	Qg (cc/min)	Gas Head (cm H2O)	krg	Qw (cc/min)	Water Head (cm H2O)	krl
1	74	12.5	0.013	35.16	11.5	0.385
1	74	12.5	0.013	33.77	11.5	0.370
1	74	12.5	0.013	29.97	11.5	0.328
2	172	13	0.030	26.51	11.5	0.291
2	172	13	0.030	27.45	11.5	0.301
2	172	13	0.030	27.19	11.5	0.298
3	172	13	0.030	24.71	11.5	0.271
3	332	13.7	0.055	26.98	11.5	0.296
3	332	13.7	0.055	29.51	11.5	0.323
3	332	13.7	0.055	20.04	11.5	0.220
4	407	12.8	0.072	12.36	11.0	0.142
4	407	12.8	0.072	9.92	11.0	0.114
4	407	12.8	0.072	11.52	11.0	0.132

7. INFERRING RESERVOIR CONNECTIVITY BY WAVELET ANALYSIS OF PRODUCTION DATA

This project is being conducted by Research Assistant Brian A. Arcedera and Prof. Roland Horne. The aim is to determine reservoir connectivity by applying wavelet analysis to production data gathered in day-to-day operations. Use of this technique could establish the degree of connectivity between wells without doing additional tests and data gathering.

7.1 BACKGROUND

In 1998, Sullera used wavelet analysis and multiple regression techniques to infer injection returns by analyzing injection rates and chloride concentrations. Her study indicated that wavelet analysis could isolate short-term signal variations which could be correlated from one well to another. The results of the study were verified successfully against tracer test data and qualitative field observations.

Sullera's study however, only demonstrated successful results from one set of field data. The other data sets she analyzed did not have sufficient data points for meaningful statistical correlations. The frequency of chloride data further hindered her analysis by limiting her to the use of monthly data. Data with monthly frequency may not be suitable for this analysis because it may not capture the short-term variations in the signal.

This project was conceived as an extension of Sullera's study. It addresses the problems of lack of data and insufficient data frequency by analyzing production data (e.g. total rate, steam rate, brine rate, wellhead pressure, enthalpy). Production data is already gathered on a regular basis for normal operating records so no additional tests or data gathering needs to be done.

7.2 METHODOLOGY

The analysis required in the study can be broken into four main steps: preprocessing, wavelet analysis, cross-correlation analysis, and multiple regression analysis. The preprocessing step rearranges the data from different sources into a uniform format for subsequent analysis. It also includes the removal of nonnumeric entries in the data and the generation of a signal over a uniform time interval. Wavelet analysis then decomposes the signal into a general trend approximation and fluctuations in the signal over different time scales. Different types of production data are then paired and analyzed in turn (e.g. injection rate vs. production enthalpy, or injection rate vs. production wellhead pressure). For a given analysis pair, detail signals from different wells are cross-correlated to determine any signal lag. The adjusted signals are then fit into a model equation and multiple regression analysis is done to determine the relative effect of each one on the others.

7.3 CONTINUING WORK

An example of a wavelet decomposition of the monthly steam production rate of a particular well is shown in Figure 7.1. The figure shows the original signal, s, followed

by the approximation, a_5, and the different details level, d_n, all plotted against the number of months elapsed. The wavelet analysis separates the general trend (declining steam production), a_5, and gives us the detail signals indicating fluctuations over different time intervals. It is these fluctuations that we hope to correlate between wells and ultimately use to determine reservoir connectivity. It is worth noting in this example that monthly data is not very suitable for our study because it may not capture short-term variations in the signal. Further, as the decomposition level goes up, the time interval we are considering increases. In Figure 7.1, for example, the detail signal at level 3, d_3, gives the signal fluctuations over a four-month period. This may be too large an interval to obtain meaningful results.
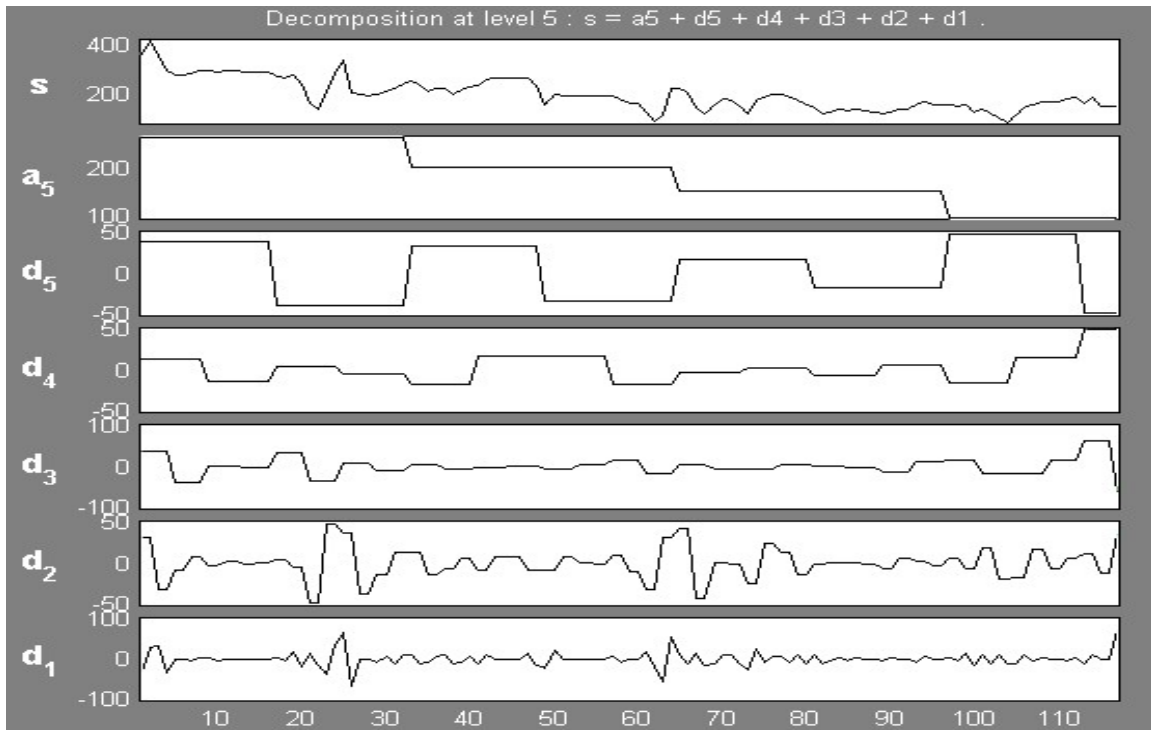
Figure 7.1: Sample wavelet decomposition of monthly steam production data.

This project is still at a very early stage and we are still in the process of gathering data and decomposing them through wavelet analysis and no correlation analysis has been done.

8. REFERENCES

Akin, S. and Kovscek, A.R.: "Imbibition Studies of Low-Permeability Porous Media," paper SPE 54590, presented at the 1999 Western Region Meeting, Anchorage, Alaska, May 26-27.

Ambusso, W.J.: *Experimental Determination of Steam-Water Relative Permeability Relations*, MS report, Stanford University, Stanford, California (1996).

Ambusso, W.J., Satik, C., and Horne, R.N.: "A Study of Relative Permeability for Steam-Water Flow in Porous Media", Proceedings of 21st Workshop on Geothermal Reservoir Engineering, Stanford University, Stanford, California (1996).

Aronofsky, J.S., Masse, L., and Natanson, S.G.: " A Model for the Mechanism of Oil Recovery from the Porous Matrix Due to Water Invasion in Fractured Reservoirs," *Trans*. AIME **213** (1958), 17-19.

Bourblaux, B.J. and Kalaydjian, F.J.: "Experimental Study of Cocurrent and Countercurrent Flows in Natural Porous Media," *SPERE* (August 1990), 361-368.

Brooks, R.H. and Corey, A.T.: "Hydraulic Properties of Porous Media," Colorado State University, Hydro paper No. 5 (1964).

Chen, J., Miller, M.A., and Sepehrnoori, K.: "Theoretical Investigation of Countercurrent Imbibition in Fractured Reservoir Matrix Blocks," paper SPE 29141, presented at the 1995 SPE Symposium on Reservoir Simulation, San Antonio, TX, Feb. 12-15.

Grant, M.A.: "Water Content of the Kawah Kamojang Geothermal Reservoir", Geothermics, Volume 8, (1979), 21-30.

Guerrero, M., Satik, C., Finsterle, S., and Horne, R.N.: "Inferring Relative Permeability From Dynamic Boiling Experiments", Proceedings of 23rd Workshop on Geothermal Reservoir Engineering, Stanford University, Stanford, California (1998).

Gupta, A. and Civan, F.: "An Improved Model for Laboratory Measurement of Matrix to Fracture Transfer Function Parameters in Immiscible Displacement," paper SPE 28929, presented at the 1994 SPE Annual Technical Conference and Exhibition, New Orleans, Louisiana, September 25-28, 1994.

Hamon, G. and Vidal, J.: "Scaling-Up the Capillary Imbibition Process from Laboratory Experiments on Homogeneous and Heterogeneous Samples," paper SPE 15852, presented at the SPE European Petroleum Conf., London, October 20-22, 1986.

Handy, L.L.: "Determination of Effective Capillary Pressures for Porous Media from Imbibition Data," Petroleum Transactions AIME (1960), Vol. 219, 75-80.

Hanselman, D. and Littlefield, B. *Mastering Matlab 5 A Comprehensive Tutorial and Reference*, Prentice-Hall, Inc.,New Jersey, 1998.

Horne R.N.: Notes on Geothermal Reservoir Engineering, Stanford University, Stanford, California (1991).

Horne, R.N., Ramey, H.J. Jr., Shang, S., Correa, A., and Hornbrook, J.: "The Effects of Adsorption and Desorption on Production and Reinjection in Vapor-Dominated Geothermal fields," *Proc*. of the World Geothermal Congress 1995, Florence, Italy, May, 1995, 1973-1977.

Horne, R.N., Satik, C., Mahiya, G., Li, K., Ambusso, W., Tovar, R., Wang, C., and Nassori, H.: "Steam-Water Relative Permeability," to be presented at World Geothermal Congress, Japan, May 28-June 10, 2000.

Iffly, R., Rousselet, D.C., and Vermeulen, J.L.: "Fundamental Study of Imbibition in Fissured Oil Fields," paper SPE 4102, presented at the 1972 SPE Annual Meeting, San Antonio, TX, Oct. 8-11.

Kazemi, H., Gilman, J.R., and El-Sharkaway, A.M.: "Analytical and Numerical Solution of Oil Recovery from Fractured Reservoirs Using Empirical Transfer Functions," paper SPE 19849, presented at the SPE 64th Annual Technical Conference and Exhibition, San Antonio, TX, October 8-11, 1989.

Leverett, M.C.: "Capillary Behavior in Porous Solids," *Trans*., AIME, **142**, 152-168, 1941.

Li, K. and Firoozabadi, A.: "Experimental Study of Wettability Alteration to Preferential Gas-Wetness in Porous Media and its Effect," *SPEREE* (April 2000).

Li, K. and Horne, R.N.: "Accurate Measurement of Steam Flow Properties," paper presented at the 1999 GRC annual meeting held in Reno, NV, October 17-20, GRC Trans. **23**.

Li, K. and Horne, R.N.: "Characterization of Spontaneous Water Imbibition into Gas-Saturated Rocks," SPE 62552, presented at the 2000 SPE/AAPG Western Regional Meeting held in Long Beach, California, June 19-23, 2000.

Ma, S., Morrow, N.R., and Zhang, X.: "Generalized Scaling of Spontaneous Imbibition Data for Strongly Water-Wet Systems," paper 95-138, presented at the 6th Petroleum

Conference of the South Saskatchewan Section, the Petroleum Society of CIM, held in Regina, Saskatchewan, Canada, October 16-18, 1995.

Mattax, C.C. and Kyte, J.R.: "Imbibition Oil Recovery from Fractured, Water-Drive Reservoir," *SPEJ* (June 1962), 177-184.

Mahiya, G.F.: *Experimental Measurement of Steam-Water Relative Permeability*, MS report, Stanford University, Stanford, Calif., 1999.

Mahiya G.F.. and Horne R.N.: "Measurements of Steam-Water Relative Permeability", Stanford Geothermal Program Quarterly Report April–June 1998, Stanford University, Stanford, California (1998).

Nathenson, M.: "Some Reservoir Engineering Calculations for the Vapor-dominated System at Larderello, Italy", U.S. Geological Survey Open-file Report 75-142, April 1975.

Pan, X., Wong, R.C., and Maini, B.B.: Steady State Two-Phase Flow in a Smooth Parallel Fracture, presented at the 47th Annual Technical Meeting of the Petroleum Society in Calgary, Alberta, Canada, June 10-12, 1996.

Persoff, P., and Hulen, J.B.: "Hydrologic Characterization of Four Cores from the Geysers Coring Project," *Proc*. of 21st Workshop on Geothermal Reservoir Engineering, Stanford, Calif., 1996.

Persoff, P., and Pruess, K.: Two-Phase Flow Visualization and Relative Permeability Measurement in Transparent Replicas of Rough-Walled Fractures, Proceedings, 16th Workshop on Geothermal Reservoir Engineering, Stanford University, Stanford, CA, Jan. 23-25, 1991, pp 203-210.

Pruess, K., and Tsang, Y.W.: On Two-Phase Relative Permeability and Capillary Pressure of Rough-Walled Rock Fractures, Water Resources Research 26 (9), (1990), pp 1915-1926.

Sanchez, J.M. and Schechter, R.S.: "Comparison of Two-Phase Flow of Steam/Water through an Unconsolidated Permeable Medium," *SPE Reservoir Engineering*, Aug. (1990), pp 293-300.

Satik, C.: "Experiments of Boiling in Porous Media", Proceedings of 22nd Workshop on Geothermal Reservoir Engineering, Stanford University, Stanford, California. (1997)

Satik C.: "A Measurement of Steam-Water Relative Permeability", Proceedings of 23rd Workshop on Geothermal Reservoir Engineering, Stanford University, Stanford, California. (1998)

Scheidegger, A.E. *The Physics of Flow Through Porous Media*, 3rd ed., University of Toronto, Toronto. 1974.

Schechter, D.S. and Guo, B.: "An Integrated Investigation for Design of a CO_2 Pilot in the Naturally Fractured Spraberry Trend Area, West Texas," paper SPE 39881, presented at the 1998 SPE International Petroleum Conference and Exhibition held in Villahermosa, Mexico, March 3-5, 1998.

Schembre, J.M., Akin, S., Castanier, L.M., and Kovscek, A.R.: "Spontaneous Water Imbibition into Diatomite," paper SPE 46211, presented at the 1998 Western Region Meeting, Bakersfield, California, May 10-13.

Sta. Maria, R.B., and Pingol, A.S.: "Simulating the Effects of Adsorption and Capillary Forces in Geothermal Reservoirs," *Proc*. of 21st Workshop on Geothermal Reservoir Engineering, Stanford, Calif., 1996.

Sullera, M.M., and Horne, R.N.: "Inferring Injection Returns from Chloride Monitoring Data", to appear in *Geothermics*, 2000.

Tsypkin, G.G., and Calore, C.: "Capillary Pressure Influence on Water Vaporization in Geothermal Reservoirs," *Proc*. of 24th Workshop on Geothermal Reservoir Engineering, Stanford, Calif., 1996.

Urmeneta, N.A., Fitzgerald, S., and Horne, R.N.: "The Role of Capillary Forces in the Natural State of Fractured Geothermal Reservoirs," *Proc*. of 23rd Workshop on Geothermal Reservoir Engineering, Stanford, Calif., 1998.

Zhang, X., Morrow, N.R., and Ma, S.: "Experimental Verification of a Modified Scaling Group for Spontaneous Imbibition," *SPERE* (November 1996), 280-285.